On the dispersion dynamics of liquid–liquid surfactant-laden flows in a SMX static mixer

Juan Pablo Valdes, Lyes Kahouadji, Fuyue Liang, Seungwon Shin, Jalel Chergui, Damir Juric, Omar Matar

On the dispersion dynamics of liquid-liquid surfactant-laden flows in a SMX static mixer

Juan Pablo Valdes[a], Lyes Kahouadji[a], Fuyue Liang[a], Seungwon Shin[b], Jalel Chergui[c], Damir Juric[c,d] and Omar K. Matar[a]

[a]Department of Chemical Engineering, Imperial College London, South Kensington Campus, London SW7 2AZ, United Kingdom
[b]Department of Mechanical and System Design Engineering, Hongik University, Seoul 04066, Republic of Korea
[c]Université Paris Saclay, Centre National de la Recherche Scientifique (CNRS), Laboratoire Interdisciplinaire des Sciences du Numérique (LISN), 91400 Orsay, France
[d]Department of Applied Mathematics and Theoretical Physics, University of Cambridge, Centre for Mathematical Sciences, Wilberforce Road, Cambridge CB3 0WA, United Kingdom

ARTICLE INFO

Keywords:
Static mixer
Two-phase flow
Surfactant-laden
Mixing
DNS

ABSTRACT

This study aims to elucidate, for the first time, the intricate fundamental physics governing the dispersion dynamics of a surfactant-laden two-phase liquid-liquid system in the well-known SMX static mixer. Following the analysis carried out in the preceding publication to this work [1], a comparative assessment of the most relevant and recurrent deformation and breakup mechanisms is conducted for a 3-drop scenario and then extrapolated to a more industrially-relevant multi-drop set-up. A parametric study on relevant surfactant physico-chemical parameters (i.e., elasticity, sorption kinetics) is undertaken, isolating each property by considering insoluble and soluble surfactants. In addition, the role of Marangoni stresses on the deformation and breakage dynamics is explored. High fidelity, three-dimensional direct numerical simulations coupled with a state-of-the-art hybrid interface capturing algorithm are carried out, which provides a wealth of information, previously inaccessible via volume-averaged or experimental approaches.

1. Introduction

Liquid-liquid (L-L) dispersions and emulsions are of central relevance to various modern industrial sectors, ranging from consumer and mass-produced goods (i.e., food, cosmetics) to processing applications (i.e., polymers, biotechnology, petro-chemical) [2]. Even though emulsions are thermodynamically unstable due to their inherent immiscibility, two criteria can be pursued to achieve a kinetic pseudo-stability: (i) addition of surface-active agents, and (ii) energy incorporation to induce drop breakage and disperse one phase into the other [2, 3]. It is well-known that surfactants play a major role in drop breakage/coalescence dynamics and the associated droplet size distribution (DSD) attained by lowering interfacial tension [4]. In turn, the dispersed phase concentration (i.e., number of drops) and DSD greatly influence, not only the emulsion physico-chemical attributes and stability, but also mixer design, operation and scale-up considerations in terms of energy requirements [2, 5].

Despite the fact that conventional high-energy methods (e.g., agitated tanks, rotor-stator mixers) remain as first choice for emulsification processes, static mixers have shown remarkable potential as an alternative to those methodologies. A static mixer consists of a series of inserts or *elements* arranged in a given configuration inside a pipe, channel, column or reactor [2]. These inserts are responsible for redistributing the flow sequentially in directions transverse to the main flow, thus inducing chaotic mixing [6, 7]. A broad range of these devices are available nowadays, and are classified according to their geometry and/or intended application, as summarized thoroughly in previous reviews [2, 7]. Static mixers are widely regarded as being more energy efficient than stirred tanks, since they guarantee a similar degree of mixing with shorter residence times, and lower capital costs and energy consumption [2, 7, 8]. These mixers have been found to distribute energy more efficiently and uniformly at a higher intensity than agitated tanks, as demonstrated experimentally by Theron et al. [9].

L-L static mixing has been extensively investigated over the past few decades, testing a broad scope of fluid properties, design and operational parameters [2]. In particular, the influence of the interfacial tension (σ), mainly through the addition of surface-active agents, has been of crucial interest given its key role in the dispersion dynamics and emulsion properties. Early works probed the effect of varying σ solely by testing different organic compounds (e.g., oils, benzene, cyclohexane), as is the case for pioneering experimental works by Middleman [10], Streiff [11], and Grace [12], who studied σ ranges between 5 - 46 mN/m, 24.7 - 46.0 mN/m, and 1 - 25 mN/m, respectively. Apart from Grace [12], who studied the physics underlying the flow and drop breakage mechanics, both Middleman [10] and Streiff [11] derived mean droplet size (D_{32}) correlations based on Kolmogorov's turbulence dispersion theory, where interfacial tension effects were accounted for through the inclusion of the Weber (We) number. Following a similar route, Berkman and Calabrese [13] studied different dispersing liquids in a Kenics mixer. Although the emphasis of this study lies in the dispersed phase viscosity, a semi-empirical D_{32} correlation was formulated, comparable to that proposed by Mid-

j.valdes20@imperial.ac.uk (J.P. Valdes)
ORCID(s): 0000-0003-3249-5194 (J.P. Valdes)

dleman [10]. All these models derived a relation of the form $D_{32} \sim \mathrm{We}^{-n}$, implying that the droplet size scales with σ.

Numerous experimental works in the following years undertook similar endeavours by proposing (semi)-empirical correlations from parametric studies [14, 15, 16, 17]. Haas [14] is among the first to report the use of surfactants in L-L static mixing and recognize the inherent complications involved, such as the possible biases when fitting coefficients for D_{32} correlations whilst assuming σ to be constant. In addition, discrepancies between σ measured in controlled lab environments vs. *in situ* values during the dispersion process are addressed, acknowledging the fact that surfactant-laden daughter droplets require a finite time to approach the equilibrium interfacial tension measured in the lab. On the other hand, Maa and Hsu [15], Legrand et al. [16] and Gingras et al. [17] carried out parametric studies on multiple fluid properties with different static mixers (e.g., SMX, helical, etc), aiming towards various applications such as micro-encapsulation [15], general oil/water dispersions [16] and bitumen emulsification [17], specifically targeting σ through the surfactant concentration. All studies maintained the same dependence of D_{32} on σ, albeit with different exponents and assuming σ to be constant [2].

More exhaustive investigations ensued on the same subject. Fradette et al. [4] correlated surfactant concentration and water-surfactant ratio with mean droplet diameter and distribution span for different mixing techniques, showing that there is not always a monotonic trend between these parameters (higher surfactant concentrations do not always lead to smaller mean diameters). In particular, it was demonstrated that the same mean droplet size (albeit with a different distribution span) can be achieved with static mixers and stirred vessels, despite the hydrodynamic differences between the two processes, attributing surface generation solely to the chemical formulation (i.e., surfactant content). Lobry et al. [6] studied four different water/surfactant/oil systems in a SMV mixer, where a noticeable change in the DSD was reported by only replacing the type of surfactant (PVA and Tween 80). It became evident that the difference between σ values at equilibrium did not truly account for the variation seen in the DSD leading to the proposition that temporal gradients in σ should be considered in relation to the residence time in the mixer. From this observation, it was argued that slower PVA diffusion times caused a higher σ during the dispersion which explained the changes in DSD observed in the experiments of Lobry et al. [6].

Das et al. [8] explored L-L dispersions in a SMX mixer at three levels of surfactant concentration, varying the superficial velocities and viscosity ratios. General trends exhibited a mean diameter decrease for reduced interfacial tensions, which was less apparent at low concentrations. A similar explanation as those conveyed by Lobry et al. [6] and Haas [14] was proposed, arguing that the dynamic σ would be higher than its equilibrium value since the interfacial concentration at a moving surface is less than that at its equilibrium, given that the rate of surfactant adsorption at the interface is diffusion-limited. Further details are given on the DSD shape at high concentrations, correlating a departure from Gaussian to log-shaped distributions with a shift in the dominant breakage mechanisms, suggesting tip-streaming as the primary one.

In addition to the studies summarised in the foregoing, an extensive array of works exist on the fundamental dynamics of surfactant-laden liquid drops in a liquid medium, mostly exploring two canonical flows: simple shear and extensional flows. In both cases, the focus is on drop deformation (in extensional [18, 19, 20] and simple shear flow [21, 22]), as well as breakage (in extensional [23, 24, 25, 26, 27] and simple shear flow [28, 29]), assuming (numerically) an insoluble surfactant confined to the interface. A few studies have accounted for surfactant solubility and scrutinized the effect of surfactant transport dynamics on the same phenomena mentioned above [30, 31, 32, 33, 34]. A number of pertinent references are cited here that have examined deforming, thinning and breaking surfactant-laden liquid threads, bridges and ligaments [35, 36, 37, 38, 39]. Although most of these works deal with a liquid-air interface, the underlying mechanisms discussed are also active in liquid-liquid systems. Essentially, all of the aforementioned studies focus on isolated and controlled scenarios where the fundamental physics can be elucidated.

To the best of the authors' knowledge, no detailed numerical studies on the intricate interfacial mechanics of surfactant-laden L-L systems have been carried out in the context of an industrially relevant operation like mixing, let alone static mixing. Instead, most studies have targeted variations in σ from a macroscopic perspective while disregarding key interfacial and bulk surfactant transport dynamics. More importantly, numerous studies have agreed on the crucial deficiencies in models assuming a constant σ, and on the substantial deviation between equilibrium vs. dynamic σ, which strongly depends on the surfactant physico-chemical properties and the dispersion process itself. Based on the above, this study seeks to provide the first account of a more realistic depiction of a L-L surfactant-laden dispersion process in a full-scale static mixing operation. For this, a framework consisting of three-dimensional direct numerical simulations coupled with a high fidelity interface-tracking algorithm will be deployed. This study will provide a wealth of information on the complex interfacial dynamics unfolding while accounting for surfactant transport at the interface and in the bulk of the dispersing phase. Furthermore, a parametric study of relevant variables, such as surfactant strength, and different sorptive kinetic profiles, will be conducted. The level of detail achieved with our numerical framework provides complementary information to that obtained via experimental studies, leading to a deeper understanding of surfactant-laden L-L dispersions in static mixers.

2. Problem formulation

This paper builds upon the results previously published by Valdes et al. [1]. Hence, the problem set-up and numerical framework remain mostly unchanged, except for the

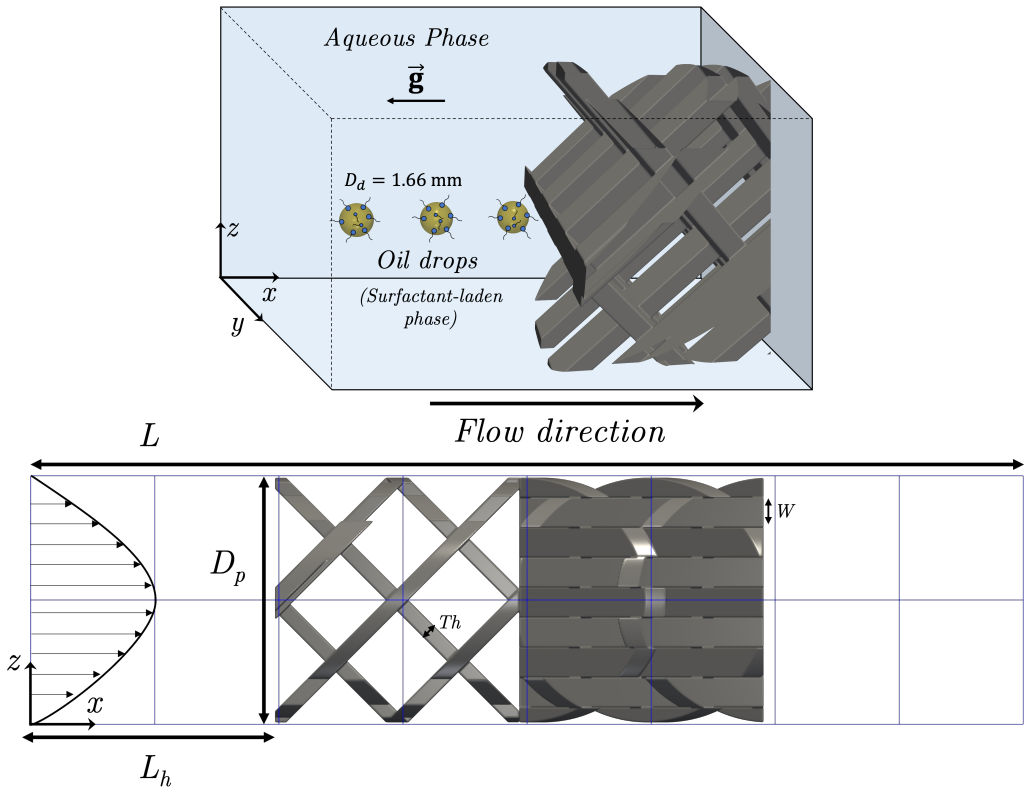

Figure 1: Problem formulation and computational domain. Top panel shows the set-up of the aqueous and oil (surfactant-laden) phases; bottom panel displays the mixer's geometry, labeling the relevant dimensions given in Table 1.

inclusion of transport equations dealing with the surfactant mass transfer dynamics. The following subsections will briefly recall the problem set-up from Valdes et al. [1] but will mostly focus on the details of the surfactant modelling. For an overview of the numerical framework employed in this study, the reader is referred to previous publications [1, 40, 41, 42].

2.1. Geometry, grid and simulation configuration

The static mixer studied herein is a 2-element standard Sulzer SMX (multi-layered) design. The mixer dimensions follow specifications given in Valdes et al. [1], which, in turn, are based on the experimental work of Liu et al. [43], as summarized in Table 1 and labeled in Fig. 1. Details of the estimation of the entrance length L_h and the numerical construction of the geometry can be found in our previous work [1]. The computational domain consists of a three-dimensional structured Cartesian grid, divided into $12 \times 6 \times 6$ sub-domains. Each sub-domain is divided into another structured Cartesian grid with a $128 \times 64 \times 64$ configuration, rendering a global mesh size of $1536 \times 384 \times 384$. The domain size is $0.064 \times 0.016 \times 0.016$ m^3 as specified in Valdes et al. [1]. Therefore, cells will have an approximate volume of 7.0×10^{-14} m^3, resulting in an average size of 4.12×10^{-5} m. As detailed in Valdes et al. [1], and validated through a grid independence study, this mesh resolution was deemed to be reliable when capturing the droplet distortion and breakup, as it complies with the number of cells per drop diameter recommended for interface-tracking algorithms [44]. Furthermore, the numerical framework used in this work naturally provides sub-grid resolution due to its front-tracking formulation (refer to § 2.2), which involves high-fidelity tracking of the interfacial dynamics occurring at smaller scales after the droplets' initial collision with the leading edge of the mixer [40].

Following the case studies mentioned in Valdes et al. [1], this paper will mostly focus on the three-drop "isolated" configuration for the dispersed phase, as depicted in Fig. 1. In this scenario, the oil droplets ($D_d = 1.66$ mm initial diameter) are at first set to be stationary and the continuous phase (denoted with subscript c) flowrate is set to $Q_c = 9.0 \times 10^{-6}$ m$^3 \cdot$s^{-1}, which renders a $Re_c = 4\rho_c Q_c / \pi D_p \mu_c = 1.63$, as specified by Valdes et al. [1]. The flow is initiated by imposing a fully-developed parabolic velocity profile at the onset of the domain as shown in Fig. 1, and no-slip boundary conditions are defined at the mixer crossbars. In addition, more complex exploratory cases with a multi-drop inlet morphology will be included. These instances will adhere to the specifications given in Valdes et al. [1] for the "Coarse Premix" case, namely 160 oil drops with a size range between $0.4 < D_d(\text{mm}) < 2$ and the same continuous flowrate Q_c.

Similarly, fluid properties are defined following the experimental tests carried out by Liu et al. [43], namely: continuous phase (aqueous solution) viscosity and density: $\mu_a = 0.615\text{Pa} \cdot \text{s}$ and $\rho_a = 1364\text{kg} \cdot \text{m}^{-3}$, respectively; dispersed phase (silicon oil) viscosity and density: $\mu_o = 0.0984\text{Pa} \cdot \text{s}$ and $\rho_o = 960\text{kg} \cdot \text{m}^{-3}$, respectively and a "clean" or surfactant-

Table 1
Geometrical specifications for the SMX mixer taken from Valdes et al. [1] and based on Liu et al. [43] tests.

Feature	
Pipe Diameter D_p (m)	0.01575
Number of Crossbars	8
Length L (m)	0.064
Aspect Ratio L_E/D_p	1
Bar Width W (m)	0.00193
Bar Thickness Th (m)	0.00102

free interfacial tension of $\sigma_{cl} = 0.036\text{N} \cdot \text{m}^{-1}$. The effects of gravity are considered acting in the negative x-direction opposite to the flow as portrayed in Fig. 1.

2.2. Governing equations

The governing equations considered in this study are presented in the context of the Level Contour Reconstruction Method (LCRM), explained in detail in previous works [1, 40, 41, 42]. Both liquid phases are treated as immiscible Newtonian and incompressible fluids. The continuity and momentum equations in a three-dimensional Cartesian domain $\mathbf{x} = (x, y, z) \in [0, 0.064] \times [0, 0.016] \times [0, 0.016]$ m can be written as follows using a single-field formulation:

$$\nabla \cdot \mathbf{u} = 0, \tag{1}$$

$$\rho\left(\frac{\partial \mathbf{u}}{\partial t} + \mathbf{u} \cdot \nabla \mathbf{u}\right) = -\nabla p + \rho \mathbf{g} + \nabla \cdot \mu(\nabla \mathbf{u} + \nabla \mathbf{u}^T) + \int_A [\sigma \kappa \mathbf{n} + \nabla_s \sigma] \delta(\mathbf{x} - \mathbf{x}_f) dA, \tag{2}$$

where t, p, $\mathbf{u}$, and $\mathbf{g}$ denote time, pressure, velocity, and gravity, respectively. The interfacial force term in Eq. 2 is decomposed into its normal ($\sigma\kappa\mathbf{n}$) and tangential components ($\nabla_s\sigma$), the former representing the mean interfacial tension and the latter arising as a consequence of interfacial tension gradients which lead to Marangoni stresses. Here, κ denotes the interface curvature, ∇_s stands for the surface gradient operator, and $\mathbf{n}$ is the normal unit vector pointing away from the interface. The 3D Dirac delta function $\delta(\mathbf{x} - \mathbf{x}_f)$ takes a value of 0 at every point except at the interface, which is located at $\mathbf{x} = \mathbf{x}_f$.

The density ρ and viscosity μ are defined throughout the domain as:

$$\begin{aligned} \rho(\mathbf{x}, t) &= \rho_a + (\rho_o - \rho_a)\mathcal{H}(\mathbf{x}, t), \\ \mu(\mathbf{x}, t) &= \mu_a + (\mu_o - \mu_a)\mathcal{H}(\mathbf{x}, t). \end{aligned} \tag{3}$$

The Heaviside function $\mathcal{H}(\mathbf{x}, t)$ given above is generated by means of a vector distance function $\varphi(\mathbf{x})$ computed directly from the tracked interface [40]. $\mathcal{H}(\mathbf{x}, t)$ is defined as zero in the aqueous phase and unity in the oil phase, with subscripts a and o denoting the aqueous and oil phases, respectively. This function is solved numerically with a smooth transition across 3 to 4 grid cells [41].

Surfactant transport was resolved in both the liquid bulk and the interface by a set of convection-diffusion equations, similar to those presented in previous works [39, 45]. It is important to mention that the surfactant is assumed to be soluble only in the oil phase, thus bulk diffusion is allowed only within the dispersed phase [42]. The surfactant concentration on the interface, Γ, is treated as follows:

$$\frac{\partial \Gamma}{\partial t} + \nabla_s \cdot (\Gamma \mathbf{u}_t) = D_s \nabla_s^2 \Gamma + \dot{S}_\Gamma, \tag{4}$$

where $\mathbf{u}_t = (\mathbf{u}_s \cdot \mathbf{t})\mathbf{t}$ stands for the tangential velocity vector in which $\mathbf{u}_s$ is the surface velocity at the interface and $\mathbf{t}$ is the unit vector tangent to the interface, and D_s is the surface diffusion coefficient. The sorptive flux accounting for the surfactant transfer between the interface and the bulk is estimated through the source term:

$$\dot{S}_\Gamma = k_a C_s(\Gamma_\infty - \Gamma) - k_d \Gamma, \tag{5}$$

where k_a and k_d are the adsorption and desorption coefficients, respectively, C_s is the surfactant's concentration in the region immediately adjacent to the interface (bulk "subphase" [45]), and Γ_∞ is the interfacial surfactant concentration at saturation. The equation dictating surfactant concentration in the bulk, C, is given as follows:

$$\frac{\partial C}{\partial t} + \mathbf{u} \cdot \nabla C = D_b \nabla^2 C, \tag{6}$$

where D_b stands for the surfactant diffusivity in the bulk. The relationship between the interfacial (Γ) and bulk (C) surfactant concentrations is governed by the source term $\dot{S}_\Gamma$, displayed in Eqs. 4 and 5, as shown in the expression below:

$$\mathbf{n} \cdot \nabla C|_{\text{interface}} = -\frac{\dot{S}_\Gamma}{D_b}. \tag{7}$$

As commonly defined in several previous works [42, 39, 45, 46], the Langmuir equation of state (EOS) is used to describe the relationship between the effective interfacial tension (σ) and the interfacial surfactant concentration (Γ);

$$\begin{aligned} \sigma &= \sigma_{cl} + \mathscr{R}T\Gamma_\infty \ln\left(1 - \frac{\Gamma}{\Gamma_\infty}\right) \\ &= \sigma_{cl}\left[1 + \frac{\mathscr{R}T\Gamma_\infty}{\sigma_{cl}} \ln\left(1 - \frac{\Gamma}{\Gamma_\infty}\right)\right], \end{aligned} \tag{8}$$

where $\mathscr{R}$ is the ideal gas constant and T is the temperature. To appropriately identify the governing forces in the system studied, all variables are rendered dimensionless through the following scalings:

$$\begin{gathered} \tilde{\mathbf{x}} = \frac{\mathbf{x}}{D_0}, \quad \tilde{\mathbf{u}} = \frac{\mathbf{u}}{U_r}, \quad \tilde{t} = \frac{t}{D_0/U_r}, \quad \tilde{p} = \frac{p}{\rho_o U_r^2}, \quad \tilde{\rho} = \frac{\rho}{\rho_o}, \\ \tilde{\mu} = \frac{\mu}{\mu_o}, \quad \tilde{\sigma} = \frac{\sigma}{\sigma_{cl}}, \quad \tilde{\Gamma} = \frac{\Gamma}{\Gamma_\infty}, \quad \tilde{C} = \frac{C}{C_\infty}, \quad \tilde{C}_s = \frac{C_s}{C_\infty}, \end{gathered} \tag{9}$$

where the tildes designate dimensionless quantities. The length and velocity are normalised by the radius of the pipe D_0, and the corresponding average flow velocity U_r at the inlet corridors between crossbars, which is calculated from the simulations carried out in Valdes et al. [1]. The interfacial surfactant concentration is scaled against the interfacial concentration at saturation (Γ_∞), whereas the concentrations in the bulk and bulk sub-phase are scaled against a reference bulk concentration (C_∞) set as an initial condition [39, 45]. As a result of this procedure, Eqs. 1 - 8 become:

$$\nabla \cdot \tilde{\mathbf{u}} = 0, \tag{10}$$

$$\tilde{\rho}\left(\frac{\partial \tilde{\mathbf{u}}}{\partial \tilde{t}} + \tilde{\mathbf{u}} \cdot \nabla \tilde{\mathbf{u}}\right) = -\nabla \tilde{p} + \frac{\tilde{\rho}}{\mathrm{Fr}^2}\mathbf{e}_x + \frac{1}{\mathrm{Re}}\nabla \cdot [\tilde{\mu}(\nabla \tilde{\mathbf{u}} + \nabla \tilde{\mathbf{u}}^T)] + \frac{1}{\mathrm{We}}\int_{\tilde{A}} [\tilde{\sigma}\tilde{\kappa}\mathbf{n} + \nabla_s \tilde{\sigma}]\delta(\tilde{\mathbf{x}} - \tilde{\mathbf{x}}_f) d\tilde{A}, \tag{11}$$

$$\begin{aligned} \tilde{\rho}(\mathbf{x}, t) &= \frac{\rho_a}{\rho_o} + \left(1 - \frac{\rho_a}{\rho_o}\right)\mathcal{H}(\mathbf{x}, t), \\ \tilde{\mu}(\mathbf{x}, t) &= \frac{\mu_a}{\mu_o} + \left(1 - \frac{\mu_a}{\mu_o}\right)\mathcal{H}(\mathbf{x}, t). \end{aligned} \tag{12}$$

$$\frac{\partial \tilde{C}}{\partial \tilde{t}} + \tilde{\mathbf{u}} \cdot \nabla \tilde{C} = \frac{1}{\mathrm{Pe}_b}\nabla^2 \tilde{C}, \tag{13}$$

$$\frac{\partial \tilde{\Gamma}}{\partial \tilde{t}} + \nabla_s \cdot \left(\tilde{\Gamma}\tilde{\mathbf{u}}_t\right) = \frac{1}{\mathrm{Pe}_s}\nabla_s^2 \tilde{\Gamma} + \mathrm{Bi}[k\tilde{C}_s(1 - \tilde{\Gamma}) - \tilde{\Gamma}], \tag{14}$$

$$\mathbf{n} \cdot \nabla \tilde{C}|_{\text{interface}} = -\mathrm{Pe}_b \mathrm{DaBi}\left[k\tilde{C}_s(1 - \tilde{\Gamma}) - \tilde{\Gamma}\right], \tag{15}$$

$$\tilde{\sigma} = \max[\varepsilon_\sigma, 1 + \beta_s \ln(1 - \tilde{\Gamma})]. \tag{16}$$

Here, Marangoni stresses, which arise from gradients in surface concentration ($\tilde{\Gamma}$), are defined as:

$$\tau_M = \nabla_s \tilde{\sigma} \cdot \mathbf{t} = \frac{\partial \tilde{\sigma}}{\partial \tilde{\Gamma}}\nabla_s \tilde{\Gamma} \cdot \mathbf{t} = -\frac{\beta_s}{1 - \tilde{\Gamma}}\nabla_s \tilde{\Gamma} \cdot \mathbf{t}. \tag{17}$$

Eq. 16 has been slightly modified by adding $\varepsilon_\sigma = 0.05$ in order to avoid negative interfacial tension values ($\tilde{\sigma}$) at high surfactant interfacial coverage ($\tilde{\Gamma} \approx 1$), as proposed by Muradoglu and Tryggvason [46]. The minimum effective interfacial tension possible with $\varepsilon_\sigma = 0.05$ lies in the same order of magnitude as experimental interfacial tension values reported for commonly used surfactants in liquid-liquid systems, such as Tween 80, PVA [6], ε - caprolactam [47], and SDS [48], in the context of static mixing applications.

The dimensionless groups appearing in the equations above are defined as follows:

$$\begin{aligned} &\mathrm{Re} = \frac{\rho_o U_r D_0}{\mu_o}, \quad \mathrm{Fr} = \frac{U_r}{\sqrt{D_0 \mathrm{g}}}, \quad \mathrm{We} = \frac{\rho_o U_r^2 D_0}{\sigma_{cl}}, \\ &\mathrm{Pe}_b = \frac{U_r D_0}{D_b}, \quad \mathrm{Pe}_s = \frac{U_r D_0}{D_s}, \quad \mathrm{Bi} = \frac{k_d D_0}{U_r}, \end{aligned} \tag{18}$$

$$k = \frac{k_a C_\infty}{k_d}, \quad \mathrm{Da} = \frac{\Gamma_\infty}{D_0 C_\infty}, \quad \beta_s = \frac{\mathscr{R}T\Gamma_\infty}{\sigma_{cl}},$$

where Re, Fr and We stand for the Reynolds, Froude, and Weber numbers, respectively. The competition between convective and diffusive surfactant transport in the bulk and at the interface is determined by the Peclet numbers Pe_b and Pe_s, respectively. The remaining parameters characterise several relevant physicochemical aspects of the surfactant species: the elasticity parameter, which acts as a measure of the "strength" of the surfactant on the effective interfacial tension exhibited, is given by β_s; the competition between desorptive capability vs. convective surface transport is accounted for through the Biot number (Bi); the ratio of adsorption to desorption rates (sorption kinetics) is given by the adsorption number (k); and the relative importance of the bulk vs. surface concentration is given by the Damkohler number (Da), commonly referred to as the adsorption depth, which can be interpreted as the characteristic depth beneath the interface that gets diluted by surfactant adsorption [31].

2.3. Scalings and parametric study outline

It is important to establish the relative importance of the governing forces and validate the proposed scalings against available experimental data. Firstly, it is useful to examine the hydrodynamics at drop scale, with $D_d = 0.00166$ m and $U_d = 0.075\ \mathrm{m \cdot s^{-1}}$ (calculated from [1]). These estimates generate values of $\mathrm{Re}_d = 0.276$, $\mathrm{Fr}_d = 0.587$, and $\mathrm{We}_d = 0.353$, which imply a heavy dominance of viscous, buoyant, and interfacial tension forces over inertia, as expected given the highly viscous and slowly flowing continuous phase through which the drops are traveling. It is worth highlighting the commanding influence of interfacial tension forces over inertia given by the low We_d obtained, as it suggests that surfactants will play a major role in the dynamics studied herein. The Re_d and We_d values obtained are well in agreement with data reported in Das et al. [8] for laminar L-L surfactant-laden dispersions in a SMX operating at $Re_c < 210$ (as defined in §2.1), where the experiments conducted lie in a range of $0.01 < \mathrm{We}_d < 1$ and $0.255 < \mathrm{Re}_d < 10.13$. Surfactant-related scalings rely on the previously mentioned pipe scale utilized for normalizing the governing equations. This involves defining length and velocity scales as $D_0 = 0.0079$ m and $U_r = 0.159\ \mathrm{m \cdot s^{-1}}$, respectively.

Both Pe values at the interface and in the bulk were excluded from the parametric study. Typical interfacial diffusion coefficients for frequently used surfactants in static mixing applications, such as SDS (Sodium Dodecyl Sulfate) [8, 48], are within a range of $10^{-12} < D_s < 10^{-8}\mathrm{m^2 \cdot s^{-1}}$ [49, 50], thus yielding a surface Peclet range of $10^3 < \mathrm{Pe}_s < 10^6$ [51], which lowers further to $1 < \mathrm{Pe}_s < 10^6$ for highly viscous solutions with dominating viscous forces (albeit assuming the same D_s as for aqueous solutions) [38]. Previous studies dealing with similar surfactant-laden systems (i.e., deforming/breaking [26] and coalescing liquid drops [51], retracting liquid ligaments [39], and liquid thread breakup [36, 37]) have hinted towards a negligible effect of increas-

ing Pe_s any further than $\sim O(10)$, suggesting that the relative importance of diffusive vs. convective transport becomes negligible for $Pe_s >> 1$ [36]. Furthermore, authors remark that the interfacial dynamics become weakly dependent on surface diffusion effects, reaching a saturation point at $Pe_s \sim O(10^2)$ [26, 39, 51]. Hence, Pe_s was set to 100, thus guaranteeing interfacial surfactant transport to be convection rather than diffusion-driven [19, 37].

The bulk Peclet Pe_b was set equal to Pe_s as suggested by Constante-Amores et al. [51] and in agreement with the numerical framework implemented in previous works [39, 45]. More importantly, setting $Pe_b = 100$ ensures the interface-bulk surfactant distribution to be kinetically-controlled by satisfying the condition $Pe_b \cdot Da \cdot Bi < 1$ [31] (except for case 9 in Table 2). Therefore, the sorption kinetics can be effectively isolated since, in this limit, the diffusive flux of surfactants onto or off the interface, driven by bulk concentration gradients, can be neglected. In other words, the diffusive timescale in the bulk will be significantly smaller than the sorptive timescales, thus instantly smoothing out bulk concentration gradients so that $C_s(t) \approx C_{bulk}$ [52]. Such a limit is appropriate for the present setup since our current grid resolution might not suffice in all cases to accurately resolve surfactant concentration gradients within the oil droplets.

The remaining surfactant-related variables included in the parametric study are grouped by the governing dimensionless parameters extracted in the previous subsection and shown in Eq. 17, namely: elasticity parameter (β_s), Biot number (Bi), adsorption number (k) and Damkohler number (Da). To effectively isolate the effect of each parameter, three sets of case studies at three levels are proposed, as summarized in Table 2. The first set (cases 1-3) corresponds to a fully insoluble scenario, where the surfactant species is effectively confined to the interface. In this way, only mean interfacial tension effects and Marangoni stresses can be appreciated at different strengths. The β_s values were selected following the ranges studied by previous relevant papers [19, 23, 39]. As a reference, in the context of this study, a $\beta_s \approx 0.7$ is representative of a system at room temperature ($T = 298.15$K) where the maximum packing concentration at the interface is $\Gamma_\infty \sim O(10^{-5})$ mol $\cdot$ m^{-2}, being on the same order of magnitude as experimental values reported for surfactants such as SDS [53, 54]. The concentration Γ_∞ was set to 1×10^{-5}mol $\cdot$ m^{-2} and kept constant throughout all case studies, taking as a reference the order of magnitude assumed for Γ_∞ in previous relevant studies [36, 51].

The second and third sets (cases 4-6 and 7-9, respectively) encompass soluble surfactants transported throughout the interface and inside the oil bulk phase. The second set explores desorptive vs. convective effects by manipulating Bi. A base case at Bi $= 1$ was defined leading to a desorptive timescale in the same order of magnitude as the one measured for SDS, which is $t_D = 1/k_d \sim O(10^{-2})$ s [55, 56]. In addition, Da set for the base case (Da $= 0.001$) results in an initial bulk concentration of $C_\infty = 1.25$ mol $\cdot$ m^{-3}, being lower than the critical micelle concentration (CMC) estimated experimentally for SDS [8]. The additional Bi values shown in Table 2 represent scenarios where the desorption kinetics have been slowed down up to $t_D \sim O(1)$ s, thus exploring a system which loses less surfactant at the interface via desorption. These cases render values up to $k_d \sim O(10^{-1})$ s^{-1}, which correspond to realistic desorption rates for surfactants such as lower alkanols and long-chain alcohols [55, 56, 57].

Table 2
Parametric study outline for all surfactant-laden cases.

Case study		β	Bi	Da	k	$\Gamma_0 \times 10^{-5}$ [$\frac{\text{mol}}{\text{m}^2}$]
1	Insoluble	0.3	N/A			0.9
2		0.6				
3		0.9				
4	Soluble	0.6	0.01	0.001	9	
5			0.1			
6			1			
7			0.1	0.01	10	0.909
8				0.1	1	0.5
9				1	0.1	0.0909

Finally, the third set explores the characteristic adsorption depth by varying Da. In order to avoid surface convection effects (constant Bi), both k and Da are varied simultaneously, adhering to the guidelines given in [45]. To achieve this, k_a and k_d are left constant, and instead, Da is conveniently modified through C_∞ and the initial interfacial concentration (see Γ_0 in Table 2). At larger Da values, C_∞ and k drop accordingly, which can be interpreted as a system with slower adsorption and/or faster desorption. The real k_a parameter defined is in the order of $O(10^3)$, and the theoretical values obtained from the k and Da numbers given in Table 2 range between $O(10^1) < k_a[\text{m}^3 \cdot \text{mol}^{-1}\text{s}^{-1}] < O(10^3)$, which agree as well with measured values for both alcohols and non-ionic surfactants [56, 57].

An important feature to consider is the role of Marangoni stresses on the dispersion and breakage dynamics taking place. Their relevance can be assessed by comparing the macroscopic flow ($t_f = \dot{\gamma}^{-1}$ [23, 58]) and drop reference timescales ($t_R = D_d/U_d$) against the Marangoni flow timescale ($t_M = \mu_o D_d/(\sigma_{cl} - \sigma)$), which essentially comes from the competition between Marangoni stress and viscous retardation [39, 51]. For this comparison, σ is taken as the lowest possible value yielded by the EOS shown in Eq. 16 (i.e., $\sigma = \sigma_{cl}\varepsilon_\sigma$), D_d, U_d are set as mentioned at the onset of this subsection, and $\dot{\gamma}$ is taken as the average value obtained in the gaps between crossbars ($\dot{\gamma} = 75 - 100\text{s}^{-1}$ [1]). In the context of this work, such comparison renders t_f, t_R (s) $\sim O(10^{-2})$ vs. t_M(s) $\sim O(10^{-3})$. Furthermore, the desorptive timescales introduced previously for the soluble cases lie in a range between $O(10^{-2}) < t_D(\text{s}) < O(1)$. Consequently, for both soluble and insoluble scenarios, Marangoni stresses will play a relevant role in the deformation and breakage dynamics since the Marangoni flow timescale can be smaller than other competing timescales in certain scenarios.

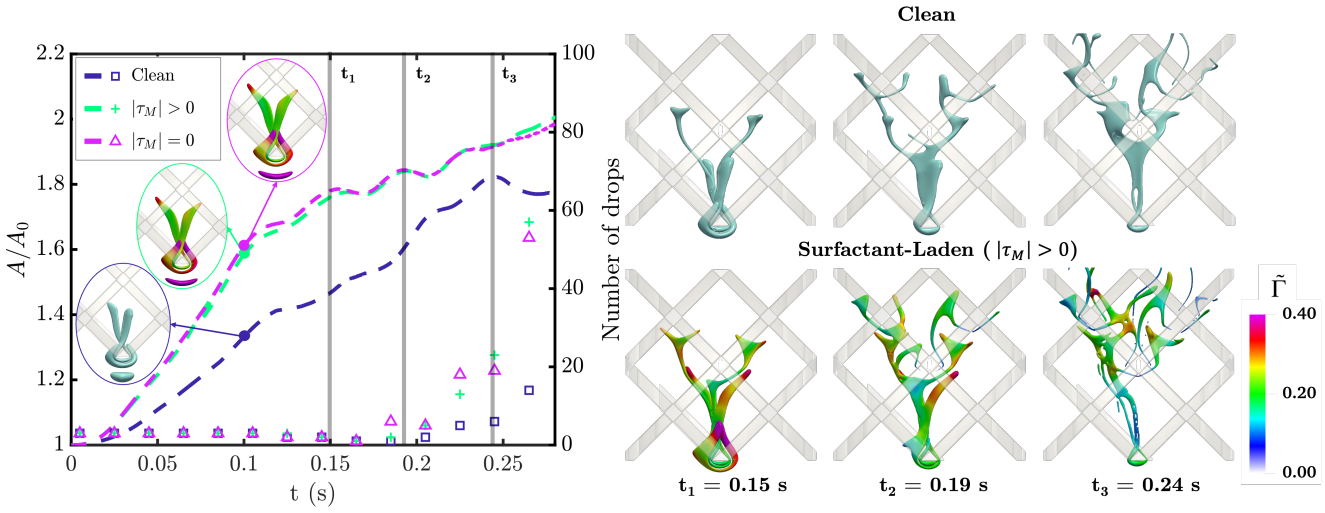

Figure 2: Comparative temporal evolution of the first stage dispersion dynamics [1] observed for the clean and surfactant-laden cases with ($|\tau_M| > 0$) and without ($|\tau_M| = 0$) Marangoni stresses. SL corresponds to Case 3 in Table 2 (insoluble surfactant with $\beta = 0.9$, $\tilde{\Gamma}_0 = 0.9$). Left axis corresponds to the dimensionless interfacial area A/A_0, plotted with dashed lines, whilst the right axis represents the number of detached interfacial structures (labeled as drops for simplicity), plotted with markers. Interfacial morphological evolution is given to the right, colored by the dimensionless surfactant surface concentration ($\tilde{\Gamma}$).

3. Results and discussion

Our numerical framework has been successfully deployed to study complex mixing applications [59, 60], and has been validated experimentally and fine-tuned (i.e., via mesh-refinement studies) for the specific SMX studied herein [1]. Moreover, the surfactant transport module has been benchmarked against multiple analytical solutions: i) uniformly expanding spheres (mass conservation), ii) non-uniform surfactant distribution in spherical surfaces (surface diffusivity), iii) drop submersion in surfactant-laden phase (bulk surfactant transport), and iv) Marangoni-driven drop migration [42]. Also, our code has been proven to accurately handle the core physical mechanics studied here (e.g., ligament retraction [39], drop coalescence [51], capillary instabilities and breakup [61]).

3.1. Surfactant-laden dispersion and role of Marangoni stresses

It is well known that higher deformation is prompted by surfactant-induced lowered interfacial tension ($\tilde{\sigma}$), as this implies lower restoring interfacial forces resisting disruptive external stresses (e.g., viscous or inertial) [18, 23]. However, the possibility of an inhomogeneous surfactant distribution at the interface leads to Marangoni stresses (τ_M) [22] whose magnitude is sensitive to the dependence of $\tilde{\sigma}$ on the local surface concentration $\tilde{\Gamma}$ ($\frac{\partial\tilde{\sigma}}{\partial\tilde{\Gamma}}$ is modulated by β and $\tilde{\Gamma}$ as shown in Eq. 17), and the local hydrodynamics, resulting in enhanced or thwarted deformation [18, 20, 26]. To identify the role played by Marangoni stress, Case 3 in Table 2 was run in two separate instances, where the tangential component of the interfacial force ($\nabla_s\tilde{\sigma}$, refer to Eq. 11 in § 2.2) was neglected in one of them (this corresponds to a 'Marangoni-free' flow situation). For conciseness, we will refer to the normal surfactant-laden and Marangoni-free cases as SL and MF, respectively. The distinct traits in the interfacial physics and breakage events unfolding between both scenarios can be directly attributed to the presence of Marangoni stresses. Selecting an insoluble configuration facilitates the analysis since only interfacial transport dynamics are involved. The upcoming discussion will be separated into two stages, as outlined in Valdes et al. [1].

3.1.1. *First stage: Deformation mechanics*

Fig. 2 quantifies the initial stage of the dispersion through the dimensionless interfacial area (A/A_0). Here, surfactant-laden cases are seen to adhere to the same behavior detailed in Valdes et al. [1] for a clean system: only interfacial distortion takes place at this stage, with essentially no breakage events being registered. As expected, surfactant-laden droplets experience a substantially larger interfacial area growth overall, quantified by the A/A_0 curves in Fig. 2, particularly at the beginning by nearly doubling the clean case stretching rate ($\frac{\Delta A/A_0}{\Delta t} \approx 6s^{-1}$ vs. $3.5s^{-1}$ @ $t = 0.1$ s, respectively). The initial wrapping, folding, and stretching motion at the leading edge, mostly governed by characteristic three-dimensional helical flows and extensional stresses [1], occurs in a similar manner for both clean and SL drops, spawning two elongating necks diverging in a v-shape (see inserts @ $t = 0.1$s on the left-hand side plot in Fig. 2).

A surprising result at first glance comes from the nearly identical evolution of the A/A_0 up to $t = 0.1$s for both SL and MF cases, suggesting that deformation mechanics at this point are not affected by Marangoni stresses, despite the elevated initial surface concentration ($\tilde{\Gamma}_0 = 0.9$). This seems to contradict previous studies [18, 20] dealing with highly tangentially-stressed drops via Marangoni stresses when exposed to extensional deformation. At a surface coverage close to saturation ($\tilde{\Gamma} \approx 1$), even with a nearly uniform sur-

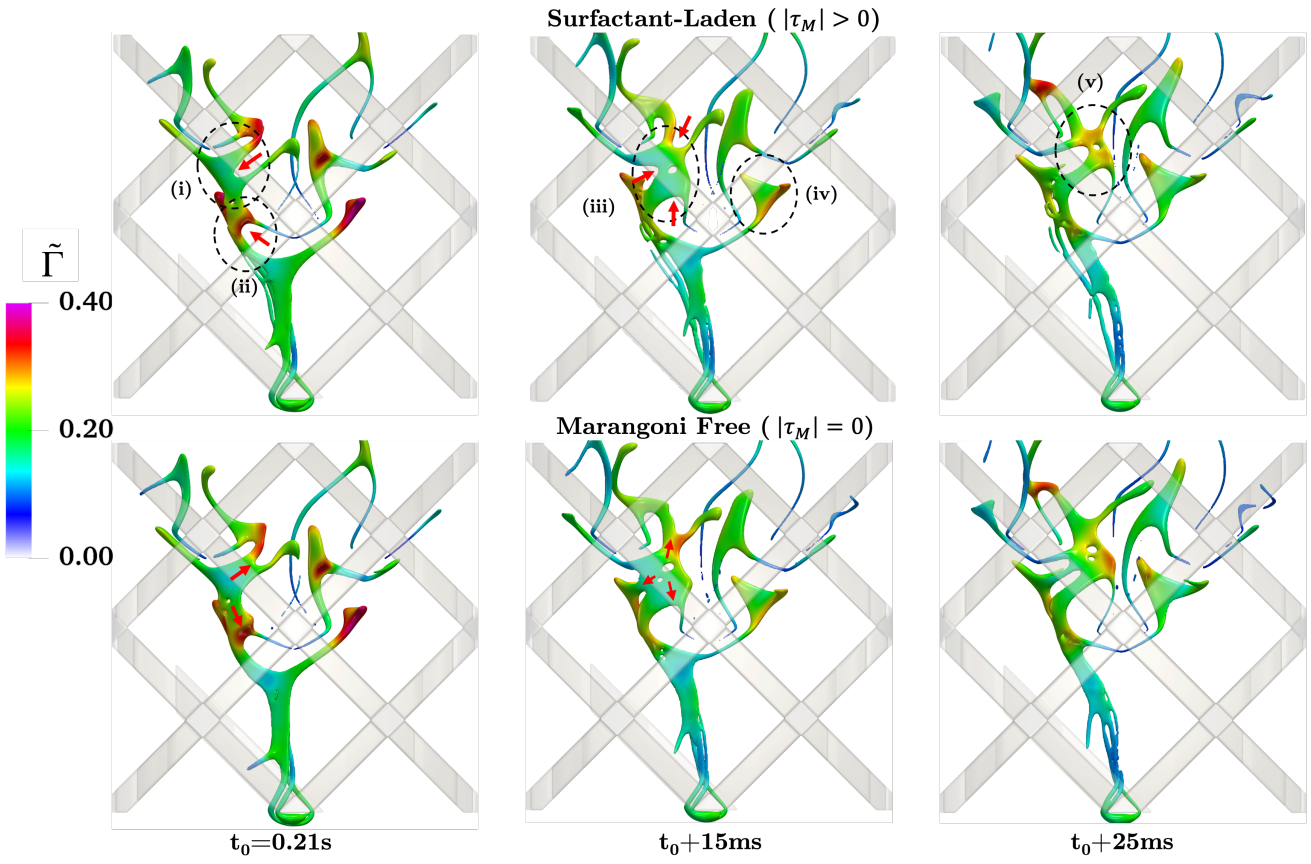

Figure 3: Comparative temporal evolution of the interface deformation with an insoluble surfactant, colored by the dimensionless surfactant surface concentration ($\tilde{\Gamma}$), for cases with ($|\tau_M| > 0$) and without ($|\tau_M| = 0$) Marangoni stresses at a constant elasticity number $\beta = 0.9$. Areas of interest highlighted in the top row to further address the role of Marangoni stresses on the deformation mechanics are presented in Figure 4.

factant distribution (i.e., small $\nabla_s\tilde{\Gamma}$) as is the case here initially, Marangoni stresses are expected to be very large in magnitude ($\tau_M \propto \nabla_s\tilde{\Gamma} \cdot \frac{\partial\tilde{\sigma}}{\partial\tilde{\Gamma}}$ with $\frac{\partial\tilde{\sigma}}{\partial\tilde{\Gamma}} \to \infty$ when $\tilde{\Gamma} \to 1$) [18, 20]. Strong τ_M implies that the deformation dynamics associated with the two cases should be at variance to some extent (e.g., τ_M can promote weak tip stretching or impede deformation by immobilizing the interface), and surfactant accumulation at the drop poles should be strongly restricted by Marangoni effects [18, 20, 23, 26]. Neither of these features are seen in the inserts at t=0.1s in Fig. 2.

To probe the early-time dynamics further, we define the flow topology parameter Q,

$$Q = \frac{\mathcal{D}^2 - \Omega^2}{\mathcal{D}^2 + \Omega^2} \begin{cases} = -1, & \text{for rotational flow} \\ = 0, & \text{for shear flow} \\ = +1, & \text{for extensional flow,} \end{cases} \tag{19}$$

where $\mathcal{D}^2 = \boldsymbol{\mathcal{D}} : \boldsymbol{\mathcal{D}}$ and $\Omega^2 = \boldsymbol{\Omega} : \boldsymbol{\Omega}$; $\boldsymbol{\mathcal{D}}$ and $\boldsymbol{\Omega}$ stand for the rate of deformation and rotation tensors, respectively [1, 60]. Converging extensional flows ($Q = 1$) have been established to drive the droplet folding motion at the leading edge, triggering the formation of necks from the elongating drop tips as they travel into the corridors between cross-bars [1]. Nonetheless, flows immediately adjacent to the leading edge are predominantly shearing in nature ($Q = 0$) [1]. This suggests a two-fold mechanism, where the drop is initially flattened and stretched via shearing stresses (up to $t \approx 0.05$s), followed by the drop tips elongating via extensional flows at the corridors.

As proposed in previous works [22, 28], Marangoni stresses exhibit limited participation in shear-induced deformation due to drop rotation, allowing significant interfacial velocities to develop (even at high $\tilde{\Gamma}$) that permit surfactant accumulation at the tips. Consequently, the initial shearing here induces two effects: 1) drop in τ_M caused by surfactant dilution as the drop expands ($\uparrow A/A_0$, $\downarrow \tilde{\Gamma}$), and 2) surfactant sweep towards the drop poles via convection [22], causing a normal stress jump (local drop in $\tilde{\sigma}$) which is compensated by an increase in curvature at the poles [20, 23]. Through this, the poles/tips elongate as they wrap around the leading edge, transitioning to the neck stretching dynamics.

Although neck stretching at $t = 0.05 - 0.1$s is governed by extensional stresses converging at the corridor, the parallel SL-MF evolution up to this point can be tied to the relevant competing timescales estimated (i.e., Marangoni t_M vs. inertia/flow t_R, t_f). Considering the definitions given in

§2.3, this comparison renders a slower τ_M timescale ($t_M \sim O(10^{-2})$ with $D_d \approx 1.05$ mm and $\sigma = 0.75\sigma_{cl}$) compared to disruptive inertia and shear stress ($t_R,\ t_f \sim O(10^{-3})$), taking as reference the strain rate experienced at the leading edge ($\dot{\gamma} = 350\text{s}^{-1}$), and the neck peak width and interfacial velocity during elongation at the corridor (@$t = 0.08$s, $U_d \approx 0.13\ \text{m}\cdot\text{s}^{-1}$, $D_d \approx 1.05$ mm). From this observation, we can infer that Marangoni stresses, which tend to hinder deformation at high $\tilde{\Gamma}$ [20, 23], are not able to act fast enough against strong disruptive inertial forces, and are eventually overwhelmed as τ_M plummets at larger deformations due to surfactant dilution ($\uparrow\ A/A_0$, $\downarrow\ \tilde{\Gamma}$, $\downarrow\ \frac{\partial\tilde{\sigma}}{\partial\tilde{\Gamma}}$) [26]. Accordingly, neck lengthening driven by strong inertia (usually at the corridor center, resulting in a nearly unidirectional elongation [1]) unfolds closely for both SL and MF. Despite concentration gradients growing as surfactant accumulates at the tips, τ_M keeps decreasing initially since $\frac{\partial\tilde{\sigma}}{\partial\tilde{\Gamma}}$ falls sharply with increasing A/A_0 at higher $\tilde{\Gamma}$. These mechanisms will hold throughout the dispersion process where either shearing stresses at the crossbars, or strong inertia in the corridors, neutralize the influence of Marangoni stresses.

As surfactant is depleted from the necks and swept towards the bulbous heads via extensional flows, tip stretching is strongly favoured, leading to a faster and flatter neck elongation compared to the clean case, spawning highly curved tips [18, 23]. At first, τ_M is not strong or fast enough to effectively restrict surface flux and prevent tip stretching, given the lower $\tilde{\Gamma}$ ($\downarrow\ \frac{\partial\tilde{\sigma}}{\partial\tilde{\Gamma}}$) [20], and strong inertia pushing the neck at the center of the corridor, as discussed previously. However, a subtle deviation in A/A_0 can be noted at $t = 0.1 - 0.15$s, corresponding to a slight neck retraction in the SL case. During this time window, elongating necks approach low-velocity recirculation zones ($Q = -1$), induced by the mixer X-shaped geometry, before forking and switching direction at the upcoming cross-point [1]. Naturally, competing Marangoni stresses grow in relevance as inertial effects weaken at these low-velocity regions, particularly when extensional deformation continues to dominate. Moreover, steady elongation prompts $\nabla_s\tilde{\Gamma}$ to rise as surfactant accumulates at the tips, which at lower $\tilde{\Gamma}$ becomes the dominant term behind Marangoni stresses.

The signature A/A_0 undulations at $t = 0.10 - 0.25$s, identified primarily as forking/wrapping mechanisms [1], are maintained between SL and MF but amplified when compared with the clean case. Similarities in the former can be attributed to shear-induced deformation driving wrapping/forking events, and strong inertial flows commanding near-unidirectional elongation in the corridor, both diminishing the τ_M effect as explored before. In contrast, increased waviness compared to the clean case comes from a lowered, in-homogeneous $\tilde{\sigma}$ inducing a more unstable interface. As captured in Fig. 2 ($t_1 - t_3$ vignettes), the SL interface tends to split and wrap at more locations without breaking, forming additional branches ($\uparrow\ A/A_0$). In addition, a larger steady deformation takes place during wrapping thanks to a $\tilde{\Gamma}$ dilution effect at the point of contact ($\uparrow\ \tilde{\sigma}$), where surfactant is swept via convection towards the nascent necks (see (iv) in Fig. 4), thus promoting further tip stretching [18, 23].

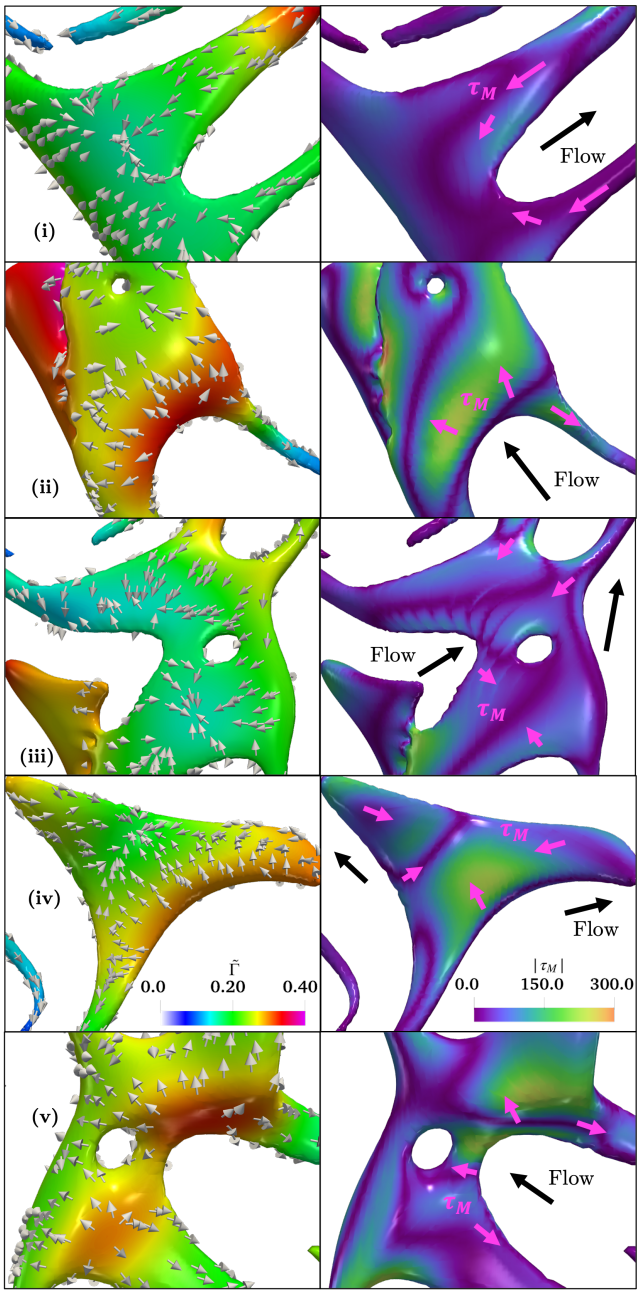

Figure 4: Closeups shown in Fig. 3. Left shows Marangoni flows through unit vectors on a $\tilde{\Gamma}$ colored interface, while right displays the magnitude of the Marangoni stresses $|\tau_M|$.

Even though the A/A_0 curves in the $t_2 - t_3$ window (Fig. 2) seem consistent between SL and MF cases, Fig. 3 highlights subtle yet key differences in the interface morphological evolution which will later impact the DSD attained (see §3.1.2). These variations arise in regions with governing extensional deformation and low flow inertial disruption (e.g., low velocity regions). Instances (i) and (iii) in Fig. 3 display an augmented interfacial retraction, where the elongating SL left branch seems tighter and less spread out, with thinner, longer, and more cylindrical necks developing. By

taking a closer look at these instances in Fig. 4, we notice that Marangoni stresses pulling inwards, opposite to the flow direction, are responsible for rigidifying the left branch tangentially as the flow attempts to stretch it, impeding nascent necks from spreading uncontrollably, but rather evolving as cylindrical columns. Deepening cavities (see red arrows in Fig. 3), absent in the MF case, progressively develop as a $|\tau_M| > 100$ threshold is surpassed around the rim of the indentation where the retraction motion ensues; τ_M here is induced by large concentration gradients promoted during early neck stretching dynamics, as analyzed above. These mechanisms help compact the expanding left branch, inducing the 'jellyfish' morphology seen in instance (v), where surfactant has been accumulated in the central ring by virtue of τ_M restricting surface flux towards the emerging branches during cavity formation (see Fig. 4 (i) and (iii)). The 'tentacles' are stabilized by reversed τ_M flows exhibited in Fig. 4 (v), going from the center outwards into the necks, in agreement with the experimental phenomena captured by Zhao et al. [62].

Similarly, τ_M also enhances interfacial retraction when acting parallel to the flow, as conveyed by close-up (ii). Although being less relevant due to larger inertial effects (higher flow velocities close to the corridor's center), Marangoni flows are sufficiently intense here (almost twice as large as instance (i)) to generate a strong surface flux that further retracts the interface, developing a more pronounced indentation than in the MF case, as seen from Fig. 3. Marangoni stresses in Fig. 4 (ii) are seen to promote surfactant transport towards the central ring region, which eventually becomes the 'jellyfish' structure described above. Nevertheless, many examples of mirrored deformations between SL and MF cases can be devised from Fig. 3, as exemplified by closeup (iv). Marangoni flows in Fig. 4 (iv) pull steadily inwards towards the center, opposite to the flow, and away from the forming poles as the wrapping motion progresses. Despite exceeding the $|\tau_M|$ threshold identified, shearing flows in the vicinity of the crossbar are dominant enough to render Marangoni action negligible, thus evolving in a nearly identical way between SL and MF. As established earlier, lower $\tilde{\sigma}$ at the tips instigates tip stretching, and the $\tilde{\Gamma}$ diluting effect at the center stabilizes the elongating structure, resulting in a larger area growth compared to the clean case. This suggests that shear-induced deformation is mostly governed by local imbalances in $\tilde{\sigma}$, prompted by $\tilde{\Gamma}$ re-distribution.

3.1.2. Second stage: breakup mechanics

The second stage of the dispersion encompasses breakage events via two mechanisms: geometrical (disruptive stress induced by the crossbars/cross-points) and hydrodynamical (capillary instabilities in ligaments) [1]. A larger number of daughter drops, as well as higher droplet birth rates, are seen for the surfactant-laden systems in Fig. 5a, akin to the A/A_0 growth rate trend discussed earlier in §3.1.1. In this case, the clean scenario production rate is nearly doubled in the presence of surfactants, with $\frac{\Delta n_{drop}}{\Delta t} \approx 1.37$ drops·ms^{-1} vs. 0.77 drops·ms^{-1}, for the SL and clean respectively, assuming a linear trend up to t_5. In addition, the SL DSD (vs. clean) carries a slightly more negative skewness (left-biased distribution with $s = -0.28$ vs. -0.16, respectively), and higher excess kurtosis (heavier tails implying higher variation from the mean with $k_{ex} = 0.49$ vs. 0.25, respectively). Despite both cases being normally distributed, as verified by standard Kolmogorov-Smirnov (KS) and Anderson-Darling (AD) tests, the altered s and k_{ex} values hint towards a generally increased production of small-sized drops with a higher degree of deviation from the mean, indicating a pivotal shift in the governing breakage physics when surfactant is added. This result is visually confirmed from the taller bars seen in the mid-to-small size range ($1\times10^{-6} < V/V_{cap} < 1\times10^{-4}$) vs. the clean case in Fig. 5b, and the left-shifted PDF and CDF curves in Fig. 5c. Even though SL and MF cases share similar trends, notable deviations in the DSD and droplet count attained can be identified in the absence of Marangoni, as we will explore further in this section.

A crucial factor influencing dispersion performance is the higher ligament population emerging in the SL case (refer to Fig. 2). Moreover, SL ligaments tend to experience a longer, more stable elongation at first, rendering them more susceptible to instabilities induced by disruptive stresses, given their larger aspect ratio ($\tilde{L}_0$) [1, 63], and naturally lower local $\tilde{\sigma}$ [21]. Deformation dynamics discussed in §3.1.1, such as increased splitting events via lower $\tilde{\sigma}$, and longer neck elongation due to a stabilized interface via $\tilde{\Gamma}$ dilution effects (e.g., during the wrapping motion), account for the surge in ligament formation with larger $\tilde{L}_0$. The same happens with the jellyfish structure generated via high extensional deformability ($\downarrow \tilde{\sigma}, Q = 1$) and rigidifying Marangoni forces. The 'tentacles', stabilized via τ_M [62], continue to elongate steadily without early breakages, thus producing large $\tilde{L}_0$ ligaments which will eventually yield more daughter drops. This agrees with studies suggesting high droplet output breakup mechanisms (e.g., tip-streaming, capillary fragmentation) to be dominant in moderately concentrated SL systems [8, 27]. Even in clean systems, elevated ligament production has been linked with higher droplet counts, since multi-drop breakup modes (e.g., capillary fragmentation) are more likely to occur at larger $\tilde{L}_0$ than binary breakups (e.g., cross-point necking or end-pinching) [1, 63, 64].

Recurrent deformation and breakup mechanisms, within the two main classifications defined at the onset of this subsection (i.e., geometrical and hydrodynamical), can be identified for the SL case in Fig. 6, and categorized as follows:

1. *Breakup via folding and necking*: Usually resulting in binary breakup, this mechanism consists of interfacial structures folding and necking at a cross-point, thanks to the flow-induced elongation of the structure extremities, and the shear stress exposure at the point of contact, giving rise to a thinning/pinching region. Depending on the cross-point location, local flow features will vary, thus leading to different outcomes. Outer cross-points prompt a steady u-shaped interfacial elongation, generating parabolic or flow-oriented ligaments, given the absence of geometrical effects on the exiting

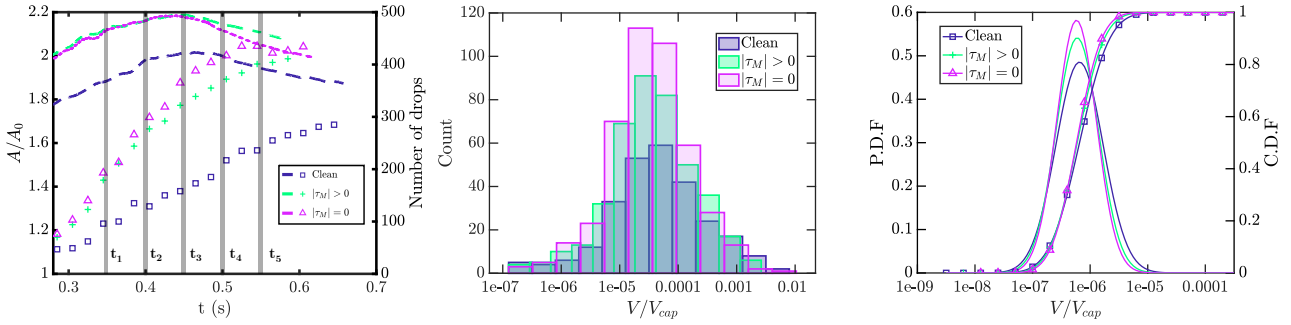

(a) (b) (c)

Figure 5: Comparative dispersion performance metrics for the clean and surfactant-laden case with ($|\tau_M| > 0$) and without ($|\tau_M| = 0$) Marangoni stresses, assuming an insoluble surfactant with an elasticity number of $\beta = 0.9$. a) Temporal evolution of the second stage dispersion dynamics as defined in Valdes et al. [1], b) overlapping dimensionless droplet size distribution (DSD) histograms, taking as a reference the capillary volume $V_c = 4\pi/3\left(\sqrt{\sigma/g\Delta\rho}\right)^3$ as in Valdes et al. [1], and c) probability and cumulative density functions (PDF and CDF). Both b) and c) figures correspond to $t = 0.59s$.

flows (Quasi-poiseuille flow at the corridor's outlet). Such is the case for ligaments #1 @ t_1, #3 @ t_2, and #4.2 @ t_3. In contrast, inner cross-points feature local swirling flow currents diverging into adjacent crossbar corridors with opposite flow directions [1]. Hence, forming filaments are either caught by recirculating regions near the crossbars, thereby initiating a wrapping process, or pulled into a corridor and stretched towards the next cross-point. Examples of this are ligament #4 @ $t_1 - t_2$, and the preceding structure from which ligaments #2 and #3 originate (not shown).

2. *Breakup via crossbar wrapping*: Similar to the previous item, this mechanism centers on the necking region developing at the crossbar through the same stress imbalance described earlier, engendering only a few daughter structures. The main difference lies in the breakup outcome. Owing to the necking region location, emerging ligaments can only stretch through parallel flow currents, as opposed to entering diverging swirling flows (i.e., at the cross-point), which could set-off further wrapping events. The wrapping structure elongates asymmetrically, contingent upon local flow conditions and surfactant-related effects (e.g., $\tilde{\sigma}$ imbalances, see §3.1.1), commonly yielding a main head and tail filament, and satellite threads. This behavior is portrayed by ligaments #2 @t_1, and #4.1 @t_2.

3. *Tip streaming/dropping*: Tip streaming occurs after a thread is drawn from a weakly deformation-resistant region (↑ $\tilde{\Gamma}$, ↓ $\tilde{\sigma}$). As surfactant gets swept towards the growing thread, local $\tilde{\sigma}$ decreases, thus triggering a necking region at the leading end [25]. A daughter drop, whose size depends on the initial $\tilde{\Gamma}$, is emitted from the pinching neck. At higher local $\tilde{\Gamma}$ and $\mathrm{Ca} = \dot{\gamma} D_d \mu_a / 2\sigma$, the thread can also neck and snap at the parent structure-thread juncture, transitioning to the tip-dropping phenomenon which results in larger daughter drops [25, 28]. Specific examples are not captured in Fig. 6 but commonly occur at the ligament bulbous lobes, where $\tilde{\Gamma}$ tends to accumulate.

4. *General pinching and capillary instabilities*: The fate of a ligament is determined by its $\tilde{L}_0$, prevailing forces acting on it (quantified through the Ohnesorge number, $\mathrm{Oh} = \mu_o/\sqrt{\rho_o \sigma D_d}$, defined at the drop scale introduced at the onset of §2.3), as well as surfactant-related effects (e.g., Marangoni). In a capillary-dominated regime (↓ Oh), breakup most likely happens via end-pinching [65]. However, depending on $\tilde{L}_0$ and Oh, a transitional regime comprising complex shape oscillations may appear, delaying or even precluding pinch-offs at the filament end, entering a middle-break mode variation [63]. In contrast, small enough ligaments (↓ $\tilde{L}_0$) entail short retraction times that inhibit instabilities from developing, thus inducing stable no-break modes [63, 65]. Filaments with sufficiently large $\tilde{L}_0$ and viscous resistive forces (↑ Oh), experience breakup via surface capillary instabilities (i.e., capillary waves), which are triggered by varicose perturbations, mimicking Rayleigh-Plateau instability [64]. Developing disturbances can be induced hydrodynamically (in tandem with inertia from the flow) or geometrically (i.e., mixer collisions). The implications of adding surfactants are manifold, as we will explore further on. Clean ligaments undergoing capillary fragmentation comply with a critical $\tilde{L}_0$ and perturbation wavelength λ threshold [1]. However, the resolution available in our simulations is not sufficient to delve further into the ramifications of adding surfactant on these critical thresholds, but further study is encouraged. Multiple examples of these phenomena can be recognized between times t_4-t_5 essentially for all ligaments tracked.

Key relationships between the listed mechanisms include the evolution from inner to outer cross-point breakup. Lig-

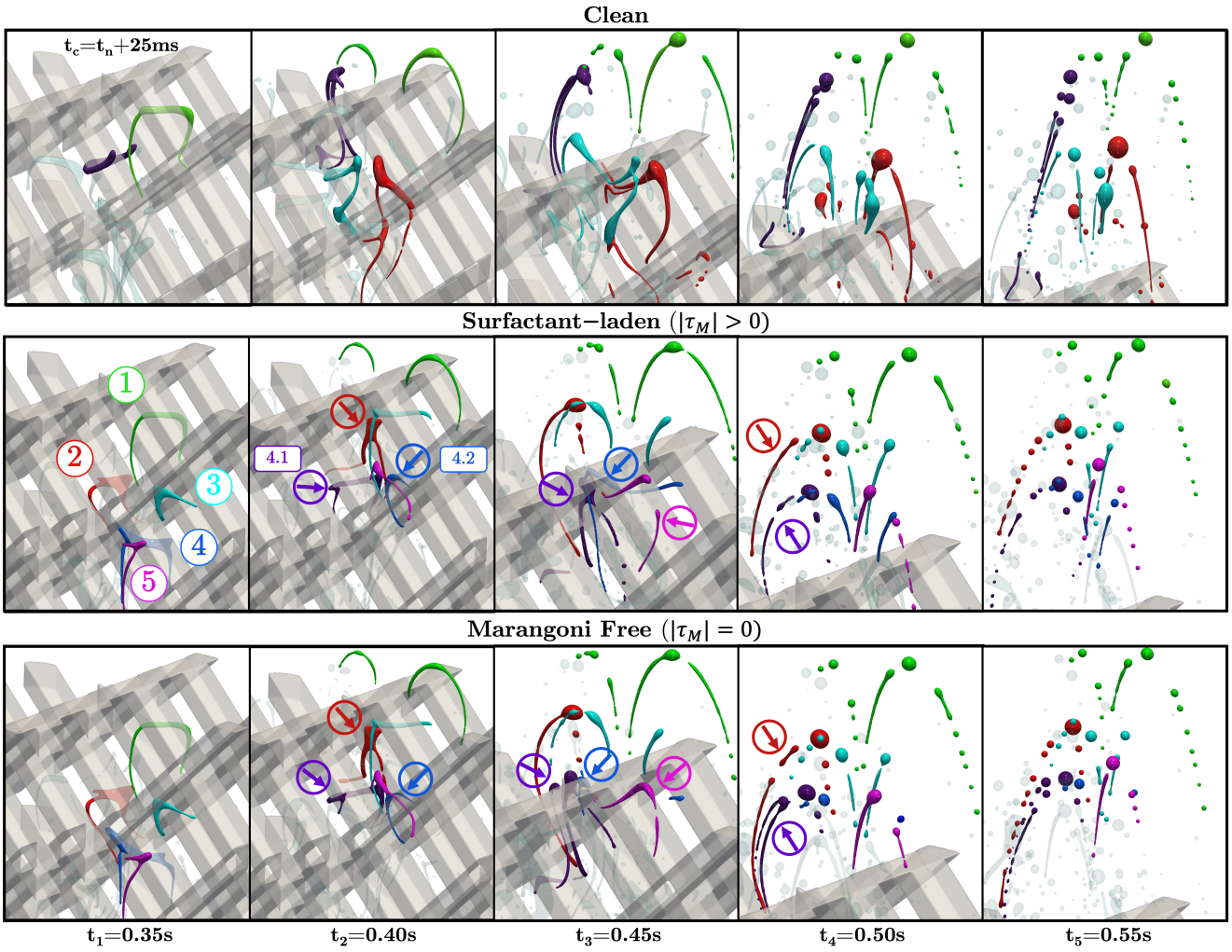

Figure 6: Comparative temporal evolution of the second stage for the clean (top), surfactant-laden ($|\tau_M| > 0$, middle) and Marangoni-free ($|\tau_M| = 0$, bottom) cases at constant $\beta = 0.9$. Five specific ligaments (color-coded) are tracked in the SL and MF scenarios to unravel recurrent breakage modes and the role of the Marangoni stresses in the breakage mechanics unfolding. Interfacial structures resembling those shown for the surfactant-laden case are highlighted for the clean with the same color code, albeit with a time delay of 25 ms to their respective counterparts. Relevant instances are pointed out through colored arrows for further discussion on particular breakup modes and their evolution, with additional detail provided in Figs. 7 and 8.

aments #3 and #4.2, both originating from an inner cross-point breakup (i.e., #4.2 spawning from #4 @ t_1), proceed to stretch into an inverted L-shape through the corridors at t_2-t_3, until they split at an outer cross-point, producing flow-oriented ligaments at t_3-t_4. Likewise, the succession from inner cross-point split to wrapping breakup can be pointed out, which incidentally connects with prime examples of fragmenting ligaments via capillary instabilities. This is the case for filaments #2 and #4.1, both emanating from an inner cross-point split. The wrapping breakages take place between $t_1 - t_2$ and $t_2 - t_3$, respectively, creating similar head and tail ligaments with neighbouring detached threads. Tip-dropping can ensue from this process at the bulging heads, given the rapid curvature increase promoted by $\tilde{\Gamma}$ and interfacial strain ($\dot{\gamma}$) accumulation ($\downarrow \tilde{\sigma}$, $\therefore \uparrow$ Ca) [20, 25]. Examples of snapped threads from the parent structure can be spotted at t_3 for ligament #4.1. Finally, elongating ligaments at t_4 (red and purple arrows) exhibit wave-like disturbances, breaking into multiple daughter drops at t_5. Ultimately, all filaments stemming from solid-interaction breakups undergo a myriad of the break or no-break modes from item 4.

Although the aforementioned physics resembles that identified for the clean case (colour coded in Fig. 6 vs. SL ligaments #1 through #3 and #4.1), multi-drop breakup modes are substantially less frequent since clean ligaments are intrinsically more deformation-resistant ($\uparrow \tilde{\sigma}$). Therefore, early steady elongation gets inhibited ($\downarrow \tilde{L}_0$), which renders them less susceptible to fragmentation via capillary instabilities. Breakage dynamics by means of cross-point necking and crossbar wrapping unfold similarly for both systems (refer to $t_{c1} - t_{c3}$ in Fig. 6), albeit with a lesser A/A_0 growth due to the lack of local $\tilde{\sigma}$ imbalances (e.g., tip stretching or $\tilde{\Gamma}$ dilution seen in §3.1.1). As a result, many nascent filaments from these events are significantly bulkier ($\downarrow \tilde{L}_0$) or struc-

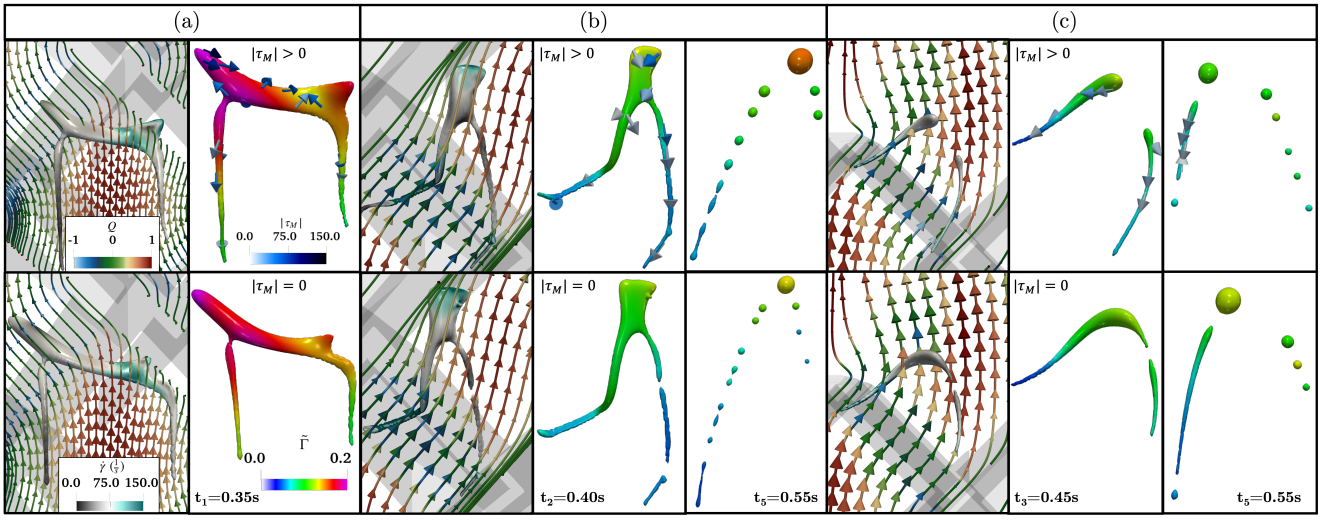

Figure 7: Comparative close-ups on several relevant ligaments at different times shown in Fig. 6 and their evolved states for surfactant-laden (top row) and Marangoni free (bottom row) cases. Per sub-figure: left view displays the deforming interface, coloured by the strain rate ($\dot{\gamma}$), embedded in flow streamlines with velocity-scaled glyphs coloured by the flow topology parameter Q. Right views depict the same interfacial structure (and its evolution when applicable) coloured by the surface concentration ($\tilde{\Gamma}$). Surfactant-laden case in the top row includes the direction and magnitude ($|\tau_M|$) of developing Marangoni flows. From left to right: a) ligament #4 (blue) at $t_1 = 0.35$s, b) ligament #2 (red) at $t_2 = 0.40$s, and its final state at $t_5 = 0.55$s, and c) ligament #5 (pink) at $t_3 = 0.45$s, and its final state at $t_5 = 0.55$s.

turally more unstable (higher capillary pressure due to $\uparrow \tilde{\sigma}$ at the thinning lobe-tail liquid bridge), thus strongly favouring either retraction or end-pinching breakups. Such is the case for the cyan and red coloured ligaments at $t_{c4} - t_{c5}$ in Fig. 6. Despite there being exceptions (i.e., purple and green ligaments deriving from wrapping occurrences $@t_{c1} - t_{c2}$), clean capillary fragmentation tends to produce lower outputs of mostly uniform (and sometimes sizeable) drops compared to the SL case. These variations in the predominant breakup modes in the presence of surfactants are reflected in the altered DSD features noted previously from Fig. 5.

Marangoni stress plays an influential role in the breakage phenomena examined, despite not being immediately evident from the comparable SL vs. MF structures depicted in Fig. 6. These similarities often stem from shear or inertia-dominated deformation where τ_M does not actively intervene, analogous to the scenarios exposed in §3.1.1. Such is usually the case for breakup mechanisms 1 and 2 (i.e., ligaments #1 and #3 $@t_1 - t_3$). However, subtle morphological differences, akin to those highlighted from Fig. 3 by virtue of τ_M, can severely impact the course of a given breakup event, as well as future breakages triggered from it (example in Fig. 7 (a) discussed up next). This, in conjunction with breakups markedly regulated by τ_M (see Figs. 7 (b-c)), lead to the performance disparity observed in Fig. 5. The MF case carries a $\approx 15\%$ higher droplet count between $t_3 - t_5$, as shown in Fig 5a, and features higher excess kurtosis ($k_{ex} = 0.73$) and lower skewness ($s = -0.12$) overall, entailing a heavily-tailed distribution with no particular bias towards larger or smaller drops, as verified from Figs. 5b, 5c. This suggests a dual nature for the Marangoni effect, where τ_M can either act beneficially (augment small droplet formation) or detrimentally (restrict droplet birth altogether). Inferring from previous discussion and further evidenced up next, Marangoni effects are simultaneously modulated by local Q, $|\tau_M|$ ($\frac{\partial \tilde{\sigma}}{\partial \tilde{\Gamma}}, \nabla_s \tilde{\Gamma}$) [18, 20], and $\mathrm{Oh} - \tilde{L}_0$ [63, 65].

Fig. 7 (a) zooms in on ligament #4 at t_1, exposed to vigorous extensional flows from below, and faint shear stresses in proximity to the cross-point, enabling active τ_M participation. Both SL and MF cases share locally equivalent restoring capillary forces ($\sim \tilde{\Gamma}$ profiles) at the point of contact. This leads to comparably high $\dot{\gamma}$ profiles in this region, heralding the onset of a necking region (inner cross-point breakup). Nonetheless, a distinctly asymmetrical elongation is captured on the left tip of the structure in the absence of Marangoni, causing a left-skewed inner cross-point split that results in a vanishing #4.2 ligament, but a dual-necking #4.1 ligament, both marked at $t_2 - t_3$ in Fig. 6 (blue and purple arrows). In contrast, strong $|\tau_M| > 100$ (over the threshold established in §3.1.1) restrict tip stretching in SL ligament #4, analogous to the retraction dynamics discussed from Fig. 4 (i-iii), leading to a middle section split. Hence, a single head and tail #4.1 filament develops at t_3 (and satellite threads), with the remaining mass going to filament #4.2, which adopts an inverted L-shape. This distinction reveals substantial implications of Marangoni effects on the fate of nascent ligaments since emerging structures akin to ligament #4.2 usually favour lower output breakup modes (i.e., outer cross-point breakup $@t_3$, followed by end-pinching $@t_5$). Instead, the MF case generates $\approx 30\%$ more drops, given the extra capillary fragmentation coming from ligament #4.1.

Fig. 7 (b) shows ligament #2 at t_2 subjected to shearing crossbar flows on the left, and extensional currents on the right, dragging the front lobe into a corridor. As expected,

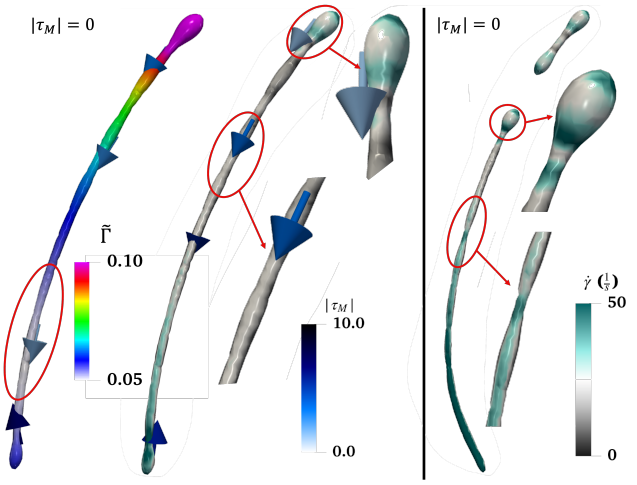

Figure 8: Close-ups on daughter ligaments at $t_4 = 0.50$s in Fig. 6 (red arrow), evolving originally from ligament #2 (red) (see t_1 in Fig. 6). Left and right correspond to surfactant-laden ($|\tau_M| > 0$) and Marangoni-free ($|\tau_M| = 0$) cases, respectively. Left view shows interfacial strain rate ($\dot{\gamma}$) and surfactant concentration ($\tilde{\Gamma}$) profiles, with the direction and magnitude of Marangoni stresses (τ_M). Right view only shows interfacial $\dot{\gamma}$.

the left segment deforms evenly at first for both SL and MF in light of weakly influential τ_M (refer to $t_2 - t_3$ in Fig. 6). On the contrary, SL's right segment develops moderate $|\tau_M| < 75$ opposing the flow, thereby diminishing strain buildup in areas exposed to extensional stress (e.g., leading head) without compromising filament elongation. This stabilizing effect promotes a longer and more stable stretching right tail which escapes early breakups, abiding by the same physics described in §3.1.1 for the necks and tentacles in Fig. 4 (i,iii,v). In contrast, MF's right tail fragments prematurely when exposed to equivalent elongational flows despite exhibiting a similar morphology ($\sim \tilde{L}_0$), therefore attributing its breakup to the lack of τ_M. This observation is consistent with previous studies arguing that surfactant depletion ($\uparrow \tilde{\sigma}$) from the thinning regions incentivizes τ_M that opposes capillary-pressure-driven flow [35], leading to reduced thread thinning rates which ultimately delay, or prevent filament pinch-off [36, 37]. Even though stabilizing Marangoni forces could favour drop production by supporting ligament lengthening ($\uparrow \tilde{L}_0$), they could also end up limiting subsequent breakups.

An example of the above comes from the evolution of ligament #2 between $t_2 - t_5$ (see Fig. 7 (b)). Marangoni two-pronged effect depends on its relative strength/activity against disruptive external stresses instigating either deformation or instability propagation. As hinted above, τ_M flows in the right tail are competitive enough radially vs. extensional stress to thwart wave perturbations, but sufficiently small and slow lengthwise to enable elongation. Analysis of the relevant interacting timescales supports this claim. Marangoni effects are on the same order of magnitude or faster ($t_M \sim O(10^{-3})$ with $D_d = 0.143$mm and $\sigma = 0.9\sigma_{cl}$) than disruptive inertia/shear stress from a radial perspective ($t_R \sim O(10^{-3})$, $t_f \sim O(10^{-2})$), taking $U_d \approx 0.073\text{m} \cdot \text{s}^{-1}$ and $\dot{\gamma} \approx 30\text{s}^{-1}$ as the average interfacial velocity and strain rate, respectively. In contrast, they appear slower overall longitudinally ($t_M \sim O(10^{-1})$ vs. $t_f, t_R \sim O(10^{-2})$ with $D_d = 3.80$mm), assuming the same U_d and $\dot{\gamma}$. However, once the right tail detaches from the parent structure and decelerates at the corridor exit, it becomes more sensitive to τ_M and less affected by external stress. Accordingly, capillary fragmentation is averted due to τ_M limiting capillary-pressure-driven flows as the filament recoils [35], which ultimately favours low drop output breakup modes ($\downarrow \tilde{L}_0$). Consequently, the SL tail yields two daughter threads at $t_2 - t_3$, whereas the early fragmented MF tail spawns three instead.

The same phenomenon is observed on the shear-disrupted left section of ligament #2 where τ_M, irrelevant at first, restricts emerging disturbances during extensional-governed prolongation at $t_3 - t_4$ (see Fig. 8). In this instance, the SL case generates over 20% less, yet slightly smaller drops ($\approx$ 10% on average) compared to MF, in agreement with the statistical traits discussed for both distributions. The average difference in drop size derives from an interplay between capillary-driven tip swelling and Marangoni-delayed end-pinching [36, 37] (see red arrows @$t_2 - t_4$ in Fig. 6). As filament #2 lengthens, its leading head bulges due to surfactant accumulation, weakly opposed by modest $\tau_M < 50$. This prompts a rise in curvature that balances the normal stress jump provoked by lowering $\tilde{\sigma}$ [20, 23], resembling the neck stretching physics addressed in §3.1.1. While the same mechanism elapses in the MF ligament, its leading lobe swiftly pinches due to the absence of stabilizing τ_M stress, and growing capillary pressure as $\tilde{\sigma}$ plummets. In this way, the MF filament engenders more, slightly larger drops, whereas the Marangoni-delayed end-pinching in the SL case allows for further oil phase to be drawn into the swelling bulbous head (reaching a higher $\tilde{\Gamma}$ as seen in Fig. 7 (b)), leading to less, but smaller nascent drops.

Fig. 8 sheds light on the nuances behind τ_M stabilizing action and its role hindering droplet birth. Thread thinning deceleration is reflected by the low $\dot{\gamma}$ profile ($<25\text{s}^{-1}$) extending through most of the SL ligament, in lieu of high strain ($\approx 50\text{s}^{-1}$) necking regions, and varicose perturbations developing in the MF filament. On top of its pinch-off retardation effort, τ_M is also noted to expedite ligament retraction by inducing inwardly converging surface fluxes. These flows arise from $\nabla_s\tilde{\Gamma}$ triggered by surfactant-depleted regions mid-ligament (see Fig. 8). Therefore, critical $\tilde{L}_0$-Oh delimiting surfactant-free no-break modes (e.g., 'short ligament' regime [63, 65]) may be altered by this effect. Kindred examples of τ_M accelerated retraction are seen for cyan and pink ligaments at t_5, spawning from filaments #3 and #5 (refer to Fig. 6 and Fig. 7 (c)). Marangoni activity scales proportionally with the local hydrodynamics, captured by $\dot{\gamma}$ (e.g., $|\tau_M| \approx 50$ influential at $\dot{\gamma} \approx 125\text{s}^{-1}$ in Fig. 7 (b), and $|\tau_M| \approx 10$ at $\dot{\gamma} \approx 25\text{s}^{-1}$ in Fig. 8).

On the other hand, Fig. 7 (c) showcases the opposite situation, where Marangoni-stabilized daughter filaments at t_3, stemming from ligament #5, attain a longer elongation ($\uparrow \tilde{L}_0$) vs. the MF case when subjected to vigorous extensional

currents, thereby breaking into more drops at $t_4 - t_5$ via capillary fragmentation. It is worth mentioning that τ_M sets SL ligament #5 into a more symmetrical initial split at $t_2 - t_3$ by immobilizing the interface, akin to the physics explored in Fig. 7 (a). Both ligaments #5 and #2 at t_3, t_4, respectively, exhibit an Oh $\sim O(1)$, implying strong enough viscous resistive forces precluding capillary-dominated breakup modes (e.g., end-pinching). However, the difference between them lies on their radial stability, quantified by the $\lambda > 2\pi R_d$ stability criterion [1]. Ligament #5 features nearly half the radius estimated for ligament #2 ($R_{d,\mathrm{L5}} = 0.66 R_{d,\mathrm{L2}}$), strongly suggesting a higher propensity for smaller λ oscillations to destabilize the filament. This accounts for the rapid breakage events seen in lieu of τ_M-enhanced retraction.

3.2. Parametric study

This section delves into the influence of handling different types of surfactants by manipulating their physicochemical nature, as delineated in §2.3 (refer to Table 2). The metrics selected to assess the mixer operation are the normalized interfacial area A/A_0, the number of detached structures or "drops" (N_d), and the DSD, represented via PDF and CDF curves. The DSD characterization is computed at $t = 0.59$s, corresponding to the earliest first drop exiting the computational domain amongst all cases (namely, case study 3 from Table 2). Accordingly, N_d is plotted between $0.2 < t(\mathrm{s}) < 0.6$. Additionally, droplet count is fitted to a generalized logistic function of the form,

$$N_d(t) = \frac{M}{1 + \mathrm{e}^{-k_g(t - t_{mid})}}, \tag{20}$$

where M, k_g, and t_{mid} are fitting coefficients indicating the function maximum value, growth rate, and x-axis midpoint value, respectively. In this way, drop breakage and overall dispersion performance can be better quantified and comprehensively analyzed for a diverse range of surfactants.

3.2.1. Effect of surfactant elasticity (β)

This subsection encompasses cases 1-3 from Table 2 where surfactants are confined to the interface, thus isolating the impact of surfactant strength (σ dependency on Γ, see Eq. 8) on the interfacial dynamics and end performance. Fig. 9 (a) illustrates a monotonic trend that remains invariant throughout the dispersion: increasing β leads to larger interfacial areas (A/A_0), which in turn implies higher A/A_0 growth rates. When surfactant is incorporated, regardless of its strength, the A/A_0 curves display similar undulations occurring between $t = 0.15{-}0.25$s, although fainter at $\downarrow \beta$. As previously inspected from Fig. 2, these undulations ($@t_1 - t_3$) correspond to additional forking/wrapping events, and longer neck elongating dynamics vs. the clean case, which seem to be sustained for all β. Furthermore, the inflection point evident in the clean case around $t = 0.25$s (see closeup in Fig. 9 (a)) is absent for all surfactant-laden cases. This point denotes the squeezing, thinning, and subsequent stretching of the initially flat and coalesced body of oil (see Fig. 2), which forks at the cross-point as the dispersion transitions to the second stage [1]. This situation is averted in the SL case given the more divaricate, already stretched, and thinned-out interfacial morphology acquired at this stage (i.e., jellyfish structure). Therefore, these observations suggest a generalization of the core deformational mechanisms exposed in §3.1.1 for lower β, albeit with a less intense effect due to stronger restoring interfacial forces ($\uparrow \tilde{\sigma}$).

Two distinct and roughly linear A/A_0 growth rates $\left(\frac{\Delta A/A_0}{\Delta t}\right)$ can be estimated for all cases during the first stage, labeled as G1 and G2 in Fig. 9 (a), respectively. These rates are associated with either early tip/neck stretching and wrapping ($@t(\mathrm{s}) \in [0, 0.15]$), or complex elongational distortion (i.e., forking/branching events) ($@t(\mathrm{s}) \in [0.15, 0.25]$). For both time intervals, growth rates scale linearly with increasing β but in a contrasting fashion. On the one hand, G1 rates rise proportionally, following a linear trend $\mathrm{G1}_\beta \approx 2.83\beta + \mathrm{G1}_{clean}$, while G2 rates drop inversely proportional to rising β, obeying the form $\mathrm{G2}_\beta \approx -1.61\beta + \mathrm{G2}_{clean}$. These relationships denote a sharper positive increment for G1 rates as β rises, whilst G2 rates decline at a slower pace. This accounts for the rapidly widening gap between curves at $t \leq 0.2$s, and the ensuing slower narrowing as we approach the transition point at $t \approx 0.25$s. This behavior points to a stronger and favorable influence of β on the early interfacial deformation dynamics occurring at G1, primarily driven by inertial or shear stresses, and consequently governed by local $\tilde{\sigma}$ imbalances (e.g., enhanced splitting and wrapping mechanics at $\downarrow \tilde{\sigma}$, see §3.1.1). Conversely, β becomes less impactful but detrimental in the latter stages, where Marangoni effects dominate over complex morphological changes (e.g., stronger τ_M rigidification at $\uparrow \beta$ suppresses interfacial spread in nascent tentacles). These trends are in agreement with several previous studies [18, 19, 23, 26] establishing two competing physical processes from the heightened $\tilde{\Gamma} - \tilde{\sigma}$ dependence $\left(\uparrow \frac{\partial \tilde{\sigma}}{\partial \tilde{\Gamma}}\right)$ at elevated elasticities: greater interfacial distortion instigated by larger $\tilde{\sigma}$ gradients (at comparable $\nabla_s \tilde{\Gamma}$), and augmented τ_M stresses inhibiting surface advection and therefore countering deformation. The A/A_0 plateaus during the second stage ($t > 0.3$s) for all cases, reaching the same value after $\beta > 0.6$, evidently hinting towards droplet birth saturation.

Fig. 9 (b) reveals a seemingly linear growing trend in the droplet count (N_d), which flattens out after $\beta = 0.6$, as gauged from the M parameters displayed in Fig. 9 (b). In contrast, the N_d growth rate does not scale linearly with β, as settled for the A/A_0, but rather jumps considerably when surfactant is added ($\uparrow \approx 40\%$ from the clean), and then remains essentially constant as β escalates, ranging between $19.14 < k_g < 19.58$. The stabilization of k_g can be verified by plotting the normalized drop count ($\tilde{N}_d = N_d/N_{max}$) against time ($\tilde{t} = t/t_f$), causing all curves to collapse to a logistic function of the form $\tilde{N}_d = \frac{0.9788}{1+\mathrm{e}^{-11.45(\tilde{t}-0.6368)}}$ with a $R^2 = 0.9955$. These features indicate a marginal effect in the predominant breakage mechanisms when varying β, since k_g remains fixed, and suggest a droplet birth saturation at increasing elasticities. Initially, one might consider

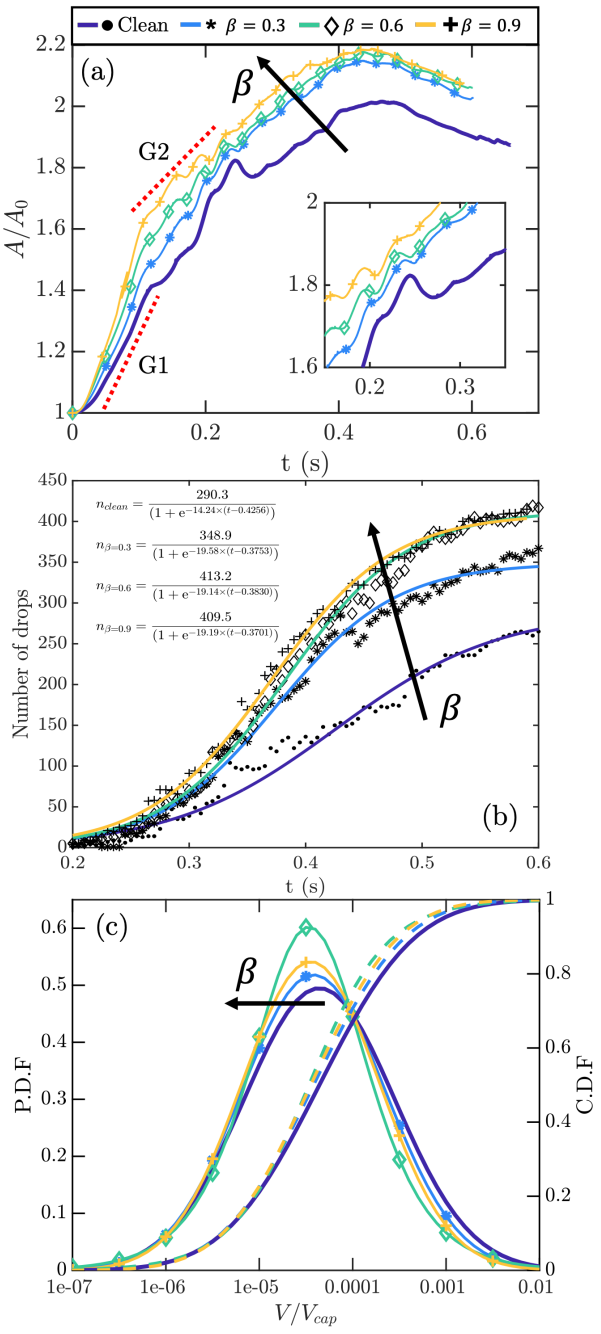

Figure 9: Comparative performance metrics for varying elasticity numbers (β). Temporal evolution of: (a) A/A_0, and (b) number of drops (markers) with generalized logistic function fittings (solid curves adhering to Eq. 20) given in the top left; (c) dimensionless DSDs, calculated as V/V_{cap} following [1], with probability (left axis) and cumulative (right axis) density functions shown. All data sets are normally distributed apart from $\beta = 0.6$, which follows a logistic distribution.

Marangoni stresses ascending in strength to be the root cause behind saturation given their stabilizing action (e.g., pinch-off retardation and escape [23, 36, 37], accelerated ligament retraction, see §3.1.2). However, MF simulations at $\beta = 0.6$ and 0.9 saturated at the same N_{max} with nearly identical DSDs, discarding a governing incidence of τ_M on this phenomena. A plausible explanation relies on the Ca_{crit} delimiting drop stability, which lowers with $\downarrow \tilde{\sigma}$. After surpassing a specific $\tilde{\sigma}$ threshold, the energy imparted by the SMX will suffice to ensure breakage ($\mathrm{Ca}_{local} > \mathrm{Ca}_{crit}$), thus implying that further lowering $\tilde{\sigma}$ will not benefit drop production, but $\uparrow \beta$ could in turn negatively impact daughter drop sizes.

DSDs in Fig. 9 (c) appear to have heavier left tails as surfactant strength increases. Nevertheless, the skewness calculated conveys a non-monotonic trend, where s rises from -0.16 to -0.39 between the clean and $\beta = 0.6$ case, but then decreases to -0.28 at $\beta = 0.9$. This is consistent with the pronounced left bias seen for the $\beta = 0.6$ PDF-CDF curves. In addition, the distributions variabilities conform to a similar pattern, always indicating a leptokurtic shape with generally wider spans at larger β, ranging between $0.19 < k_{ex} < 0.79$. This denotes a higher drop production leaning toward smaller sizes but exhibiting amplified variability with increasing surfactant strength, aligning with the trends explored in Fig. 5. By dissecting the raw data, $\beta = 0.6$ manifests a surge in medium-sized drops ($V/V_{cap} \sim O(10^{-4})$), resulting in a substantially heavier left tail and thereby transitioning to a logistic distribution. Instead, $\beta = 0.9$ reveals a comparatively augmented population of large and small entities (i.e., normally distributed). This suggests an adverse impact on the breakage dynamics when β values exceed saturation, given that stronger τ_M stabilizing effects would facilitate the preservation of larger drops. This agrees with previous experimental observations [8], where a departure from Gaussian-shaped distributions was attributed to a shift in the prevalent breakup modes. Despite these discrepancies, a non-parametric Kruskal-Wallis test (conducted due to the violation of normality and homoscedasticity [1]) demonstrated no statistically significant differences in the mean ranks between DSDs, thus hinting towards a low impact of varying β in the governing breakup physics.

3.2.2. *Effect of surfactant desorption vs. convection*

This subsection comprises cases 4-6 in Table 2, where surfactant is no longer confined to the interface and can be transported freely into the bulk (oil) phase. Its desorptive capability is manipulated through k_d, and its characteristic timescale is compared against surface convection through the Bi number, as addressed in §2.3. Similar to the results given in §3.2.1, Fig. 10 (a) conveys a consistently monotonic, although inversely proportional tendency: A/A_0 diminishes as surfactant desorption is enhanced ($\uparrow$ Bi). Unlike the insoluble scenarios, the signature A/A_0 undulations ($@t = 0.15 - 0.25$s) are drastically reduced with augmenting surfactant solubility, resembling those seen for the clean case. Moreover, the inflection point established at $t = 0.25$s, signaling stage transition, is partially recovered at the strongest desorptive capability simulated (Bi=1), as captured in the closeup vignette in Fig. 10 (a). Both features indicate a pivotal shift in the deformation dynamics unfolding in the first stage vs. insoluble and weakly soluble surfactant-laden cases. As expected, heightened desorption eliminates surface concentration gradients ($\nabla_s \tilde{\Gamma}$) by preventing surfactant buildup

(e.g., at the leading lobes during neck stretching), thus rendering Marangoni effects negligible and consequently inhibiting τ_M-driven mechanisms (e.g., jellyfish formation via interfacial retraction and rigidification). The A/A_0 saturates during the first stage ($t < 0.25$s) at Bi≤0.1, overlapping with the insoluble curve at Bi=0.01, suggesting that the impact of solubility on convection becomes negligible thereafter.

These observations are consistent with previous studies, confirming that elevated surfactant mass transfer into the bulk leads to deformations between those developed by clean and insoluble surfactant systems [30, 31]. This is attributed to the concurrent reduction of $\tilde{\Gamma}$ and $\nabla_s\tilde{\Gamma}$, suppressing both inhomogeneities in capillary forces ($\uparrow\ \tilde{\sigma}$) and Marangoni stresses, thereby mitigating many of the phenomena discussed throughout this work. These dynamics arise from the inherent compensating effect induced by solubility, where surfactant is adsorbed in regions of low $\tilde{\Gamma}$ and desorbed in regions of high $\tilde{\Gamma}$ [30] (modeled via Eq. 5). In addition, A/A_0 exhibits a monotonic descent with ↑ Bi given the constant adsorption-desorption ratio maintained through cases 4-6 (see k in Table 2), hence preventing preferential sorptive effects from counteracting the competition against surface convection (e.g., adsorption supplying surfactant-depleted regions faster than desorption removing $\tilde{\Gamma}$ accumulation, permitting greater distortions at high solubility due to $\downarrow\tilde{\sigma}$ [31]).

The A/A_0 growth rate linear approximations carried out in §3.2.1 (labeled as G1 and G2 in Fig. 9 (a)) can be replicated here. In contrast to the insoluble scenarios, growth rates G1/G2 do not scale linearly with varying desorption, but rather obey a quadratic dependence on the logarithm of Bi, expressed as $G_{Bi} = f(x^2) = f(\log(Bi)^2)$. Nonetheless, G1 and G2 retain a divergent behavior with respect to Bi, analogous to the correlation established for β but in an opposite manner given the inverse A/A_0 - Bi dependency. In this case, G1 rates diminish quadratically with rising $x = \log(Bi)$ at a rate of $\frac{dG1}{dx} = -0.4416x - 0.9548$, whilst G2 rates escalate in the same fashion at a rate of $\frac{dG2}{dx} = 0.3166x + 0.4902$. A sharper decline for G1 and a smoother rise for G2 can be inferred from the above ($|\frac{dG1}{dx}| > |\frac{dG2}{dx}|$), generating the same rapid gap widening at $t \leq 0.2$s and subsequent slower narrowing detected in Fig. 9 (a). These trends point towards a substantial influence of desorptive kinetics on the early inertia/shear-governed deformational dynamics, given the fast-paced $\tilde{\sigma}$ homogenization that transpires as $\tilde{\Gamma}$ plummets. Neck formation is heavily limited at higher Bi, favoring early coalescence (i.e., after the leading edge) which leads to an interfacial structure resembling that of the clean system (see t_3 in Fig. 2). Latter distortion ($t > 0.15$s) slightly intensifies at high Bi given the mostly uniform $\tilde{\Gamma}$ profiles attained early on. This homogeneity eliminates concentration gradients, thereby negating the effects of τ_M on interfacial spread, contrary to the findings discussed in §3.2.1 for ↑ β.

Fig. 10 (b) portrays a lowering trend for the final droplet count with increasing Bi, starting from saturation at Bi=0.01 and holding a linear relationship against log(Bi). However, a larger gap (↓ 23%) exists between Bi=1 and the clean case, hinting towards highly desorptive scenarios (Bi>1) where

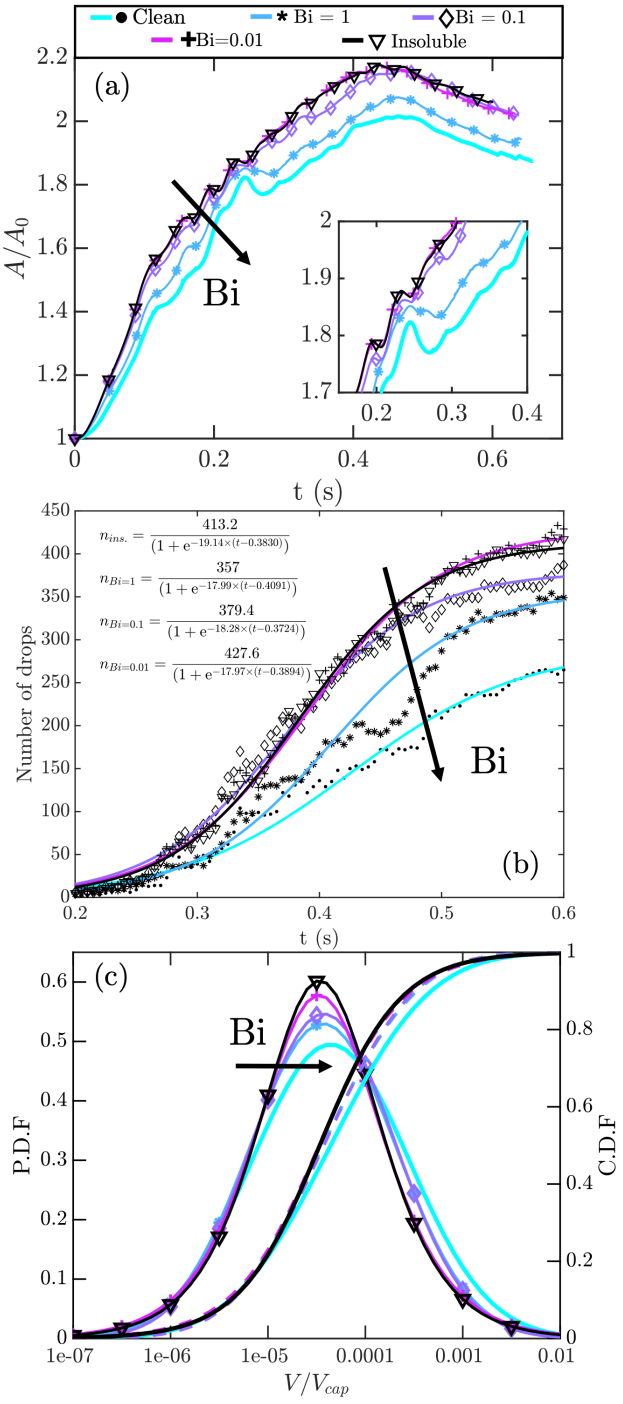

Figure 10: Comparative performance metrics for varying Bi. Same description given in Fig. 9 applies, with all cases being normally distributed, except the insoluble and Bi=0.01 case.

drop production could still surpass that of a clean system. The N_d growth rate rises when surfactant is added (↑≈ 26%) and remains stable for all soluble scenarios, with values amidst $17.97 < k_g < 18.28$. Nonetheless, breakage mechanisms can not be claimed to remain consistent at different Bi from the k_g invariability among cases, as concluded for the insoluble scenarios. An attempted collapse of $\tilde{N}_d$ vs. $\tilde{t}$ for all Bi values further clarifies this insight. This procedure yields a

logistic regression $\tilde{N}_d = \frac{0.9735}{1+e^{-12.92(\tilde{t}-0.6447)}}$, where Bi=1 conforms with a higher level of deviation ($R^2_{\text{Bi=1}} = 0.96$ vs. $R^2 > 0.99$ for Bi<1). This discrepancy appears at t(s) $\in$ [0.4, 0.5] in Fig. 10 (b), where N_d uncharacteristically falls below the logistic fit. To account for the possible variations in the breakage mechanisms, we must bring forth notions explored in §3.1.2, such as restricted ligament formation and elongation due to $\uparrow \tilde{\sigma}$ and $\downarrow \tau_M$, which could potentially cascade into favouring low output breakup modes and also tamper with developing capillary instabilities. Previous studies agree with these observations as they have demonstrated that neck formation and rate of thinning markedly fluctuates as a function of Bi and surfactant coverage [32]. Further detail into the altered deformation and breakup dynamics in these scenarios could certainly be dissected in future studies.

DSDs in Fig. 10 (c) generally indicate a left bias and wider span compared to the clean, regardless of the surfactant's desorptive activity. This is confirmed by the s and k_{ex} parameters, which often convey a more pronounced negative skewness ($-0.1093 < s < -0.4422$, with Bi=0.1 being the exception), and always confer leptokurtic shapes with larger k_{ex} ($0.4701 < k_{ex} < 0.6168$). Similar to the conclusions in §3.2.1, adding surfactant promotes the production of smaller daughter droplets but introduces a larger degree of variability. It is worth noting that even at the strongest solubility tested (Bi=1), surfactants continue to exert a significant influence on the DSD attributes, resulting in the highest k_{ex} amongst all Bi cases. This comes from the interplay of competing breakup dynamics, alternating between those identified for the clean and SL case in §3.1.2. On the other hand, a Kruskal-Wallis test unveiled statistically significant differences between the insoluble and highly desorptive cases (Bi>0.01), whereas the clean and soluble showed no significant differences except for the weakly soluble scenario at Bi=0.01. Furthermore, DSDs are seen to depart from Gaussian shapes as we approach the insoluble limit (Bi=0.01), confirming that rising desorption capability alters significantly the predominant breakup modes [8], drifting towards the mechanics elucidated for the clean case.

3.2.3. Effect of surfactant adsorption depth

This subsection encompasses cases 7-9 from Table 2, varying simultaneously Da and k as indicated in [45]. The solubility analysis here focuses on the surfactant sorption kinetics, considering varying adsorption 'depths' below the interface from which surfactant can be retrieved from the bulk phase [31]. A higher solubility is given by $\uparrow$ Da, $\downarrow k$, denoting smaller adsorption depths and thereby comparatively weaker adsorption vs. desorption kinetics. As mentioned in §2.3, k_a is not varied directly, but rather Γ_0 and C_∞ for numerical convenience. This procedure generates systems where the actual feature being manipulated is the relative importance of Γ and C. Considering this approach, connections to the underlying physics explored throughout §3.1 will not be emphasized as most come from the immediate effect of lowering or increasing $\tilde{\Gamma}$. Nonetheless, these cases can also be interpreted via Da and k as equivalent surfactant-laden mixtures with varying sorptive natures. Consequently, the findings explored in this subsection can not be directly tied to the sorption kinetics but do provide insights on the possible behaviour of self-similar systems.

Fig. 11 (a) illustrates comparable trends to those addressed in §3.2.2, exhibiting the same monotonic and inversely proportional relationship between A/A_0 and Da. As discussed previously, higher surfactant solubility causes a severe reduction of the A/A_0 undulations at $t = 0.15 - 0.25$s and a recovery of the stage-transitioning inflection point at $t = 0.25$s. However, rising Da and dropping k has a more dramatic effect than elevating desorption through $\uparrow$ Bi, as evidenced by the highly soluble case at Da = 1, which closely aligns with the clean A/A_0 curve and fully restores the inflection point. Although these results are mostly due to the initially low surface concentration ($\Gamma_0 \approx \frac{\Gamma_\infty}{10}$ see Table 2), they can be interpreted as a more substantial influence of adsorption strength on $\tilde{\Gamma}$. This stems from k being lower than unity ($k = 0.1$ for Da = 1), representing a surfactant whose desorption rate is faster than its adsorption (weakly adsorptive). For this reason, regardless of other competing transport dynamics (e.g., surface convection or diffusion), surfactant pivots towards desorption and accumulation in the bulk phase, thus rendering a deformational profile closely resembling that of the clean case. In contrast, all Bi cases in §3.2.2 maintained $k > 1$ (highly adsorptive), which could account for the less impactful effect of increasing desorption. A near saturated state is reached at Da = 0.01 (overlapping with the insoluble curve), hinting towards a negligible impact of further lowering Da / rising k thereafter.

The A/A_0 growth rates (G1,G2) adhere to a similar behavior as the one settled for Bi in §3.2.2 by obeying a dependence, albeit linear in this case, against the logarithm of Da. G1 and G2 rates hold opposing behaviors against $\uparrow$ Da, $\downarrow k$, with G1 rates decreasing at a faster pace compared to that at which G2 rates rise, following linear expressions of the form $G1_{Da} \approx -0.6272 \cdot \log(Da) + G1_{Da=1}$ and $G2_{Da} \approx 0.2475 \cdot \log(Da) + G2_{Da=1}$, respectively. Accordingly, rapidly declining G1 rates lead to a widening gap between curves at $t \leq 0.2$s, whilst slowly ascending G2 rates provoke a narrower disparity. Nonetheless, these responses result marginally different than the ones identified in §3.2.2, given the linear nature at which growth rates scale. If we interpret these systems from an adsorptive profile perspective, the general deformation dynamics unfolding during the first stage will be analogously affected with increasing solubility as evaluated for the Bi cases (i.e., highly limited neck formation and weak τ_M-driven retraction due to uniform $\tilde{\Gamma}$). However, these mechanisms evolve slower than those in §3.2.2 for $\uparrow$ Da given their linear scaling, rendering them independent of the surfactant's sorptive profile.

Fig. 11 (b) depicts a flat droplet count profile for Da $\leq$ 0.1 and a sudden drop at Da=1. Even though the M parameters do not converge between the clean and highly soluble case (Da=1), they do not exhibit a major jump akin to that calculated for Bi=1 in §3.2.2 ($\approx$ 15% drop from Da=1). From this, we can safely estimate an upper bound of Da $\sim$

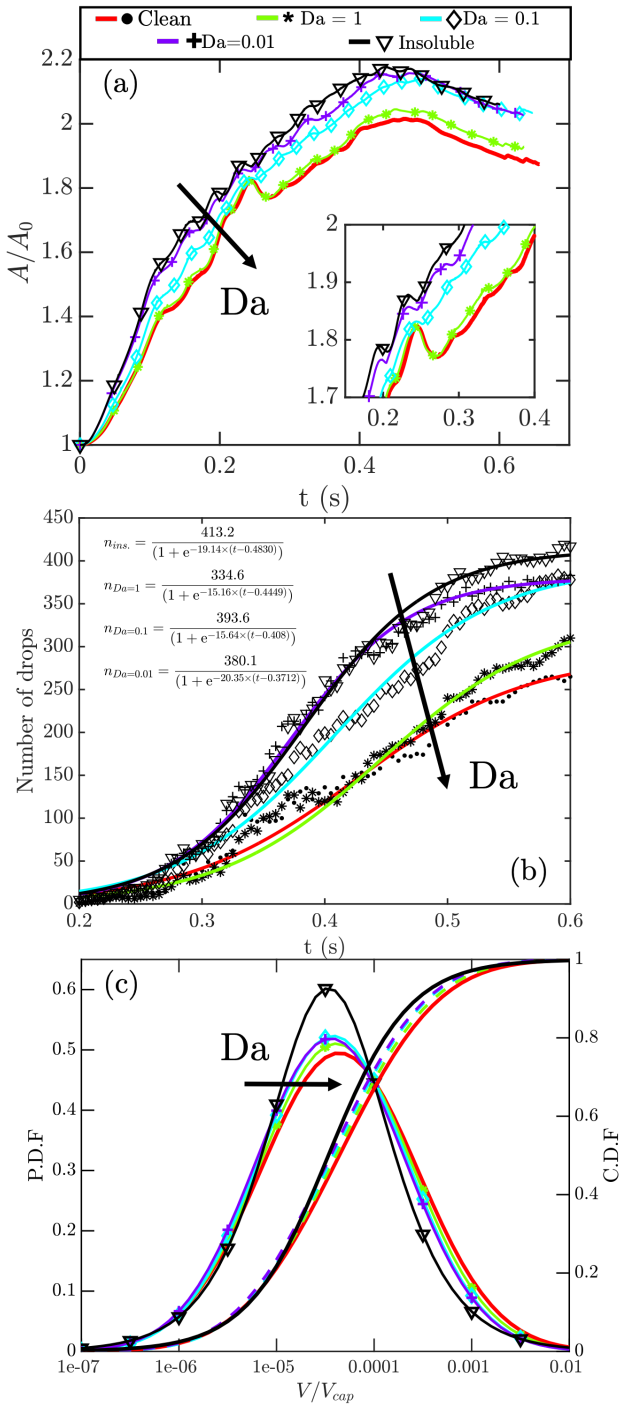

Figure 11: Comparative performance metrics for varying Da. Same description given in Fig. 9 applies here. All cases, except the insoluble case, are normally distributed.

$O(10)$ where the generalized dynamics would collapse to those unfolding in a clean mixture, specially since this would yield a system with $k \sim O(10^{-2})$ where surfactant would be essentially irreversibly lost to the bulk phase once it gets desorbed. Contrarily to §3.2.2, k_g values remain virtually unchanged from the clean to the moderately soluble cases up to Da=0.1. The abrupt spike occurs at Da=0.01, where k_g surges by $\approx 30\%$, leveling with the insoluble case. This result potentially reinforces the premise postulated from Fig. 11 (a), hinting that adsorption strength plays a highly influential role on Γ, thereby swiftly altering the mechanisms governing breakage. By performing the same N_d vs. t normalisation at varying Da, a logistic regression of the form $\tilde{N}_d = \frac{0.9749}{1+e^{-13.12(\tilde{t}-0.6456)}}$ is obtained, where Da ≥ 0.1 cases fit with a lower accuracy ($R^2_{\text{Da=0.01}} = 0.99$ vs. $R^2 < 0.97$ for Da>0.1). This deviation can't be clearly distinguished from Fig. 11 (b), but emulates the behavior seen for Bi=1, where the droplet count falls below the general logistic fit around $t(\text{s}) \in [0.35, 0.55]$. These observations can be interpreted as a sharper transition between clean and SL breakup modes at different k, unlike the interplay between co-existing modes proposed in §3.2.2 at different Bi.

The PDFs shown in Fig. 11 (c) depict similar tendencies to those explored in §3.2.2, with a generalized left-bias and broader variability with decreasing solubility. The k_{ex} and s parameters (estimated from the raw data) convey a slightly different story. The system at Da=1 yields $|s| < |s_{clean}|$ and a $k_{ex} < k_{ex,clean}$, indicating a near-normal DSD with a low dispersion from the mean. This case remains uninteresting as discussed before due to its close resemblance to the clean system ($\Gamma_0 << \Gamma_\infty$). On the other hand, cases above Da=0.1 reveal a substantially different behaviour. The raw data unveils an abnormal surge in the production of medium-sized interfacial structures ($V/V_{cap} \sim O(10^{-4})$) for the moderately soluble scenario (similar to the insoluble $\beta = 0.6$ case), whereas the weakly soluble system evenly distributes drops among $O(10^{-5}) < V/V_{cap} < O(10^{-3})$, dragging the k_{ex} and s features down. As postulated previously, this trend could indicate a sharp transition in the governing breakup modes when the adsorptive profile is modified, suggesting it has a more commanding influence on the underlying physics than enhancing desorption with a constant k profile.

As a closure to §3.2, Fig. 12a displays the shape of selected DSDs through a kernel density estimation (KDE), visually presented via violin plots. A weak bi-modal nature of the clean DSD becomes immediately evident, with two distinct peaks located in the interquartile range (IQR), probably due to dominant low output breakup modes of bulkier structures (see §3.1.2). Interestingly, this feature is promptly eliminated and the DSD characteristics are noticeably altered when incorporating surfactant, even at the highest solubility trialed (Da=1) despite producing a similar drop count to the clean system. As surfactant activity increases, either via higher β or weaker solubility, the IQR markedly tightens and the mean lowers whilst maintaining relatively long lower tails, indicating a pivotal shift in the predominant breakup modes, and accounting for the generally larger k_{ex} and prominent left skewness detected in most SL cases. Accordingly, the IQR could serve as a potential indicator of surfactant activity in the system. Large interfacial structures ($V/V_{cap} > O(10^{-3})$) survive at moderate solubility given the active competition with clean breakup modes (see §3.1.2), whereas the upper tails shrink for the insoluble cases.

Furthermore, Fig. 12b provides a summary of the overall relationships dissected throughout §3.2 based on the max-

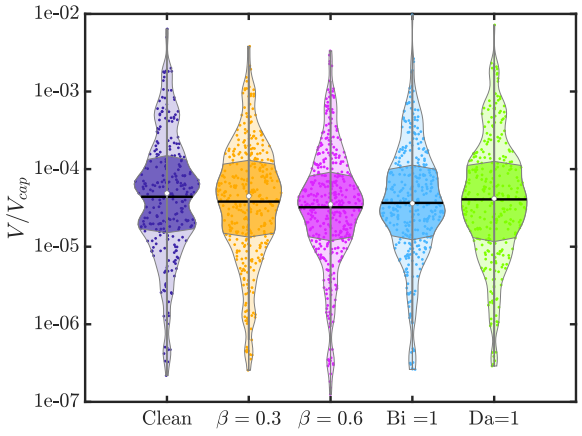

(a)

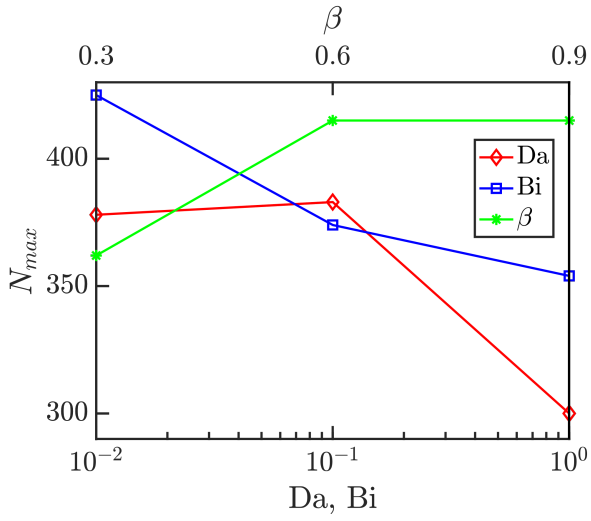

(b)

Figure 12: Global comparisons between selected cases. (a) Dimensionless DSD violin plots. Kernel density estimation considers a constant bandwidth, following the well-established Silverman [66] rule of thumb for normally distributed data-sets. Interquartile range (IQR) is given by the shadowed region in each violin. Mean and median values are depicted by black horizontal lines and white dots, respectively. Grey "whiskers" represent the $1.5 \times$IQR limit, (b) global maximum drop count (N_{max}) attained by each case throughout the dispersion.

imum droplet count (N_{max}) attained. N_{max} increases until saturation with ascending elasticity, and decreases with strengthening solubility. However, the descending profile differs depending on the manipulation given to the sorption kinetics, with N_{max} exhibiting a convex and concave shape for increasing Bi and Da, respectively. These behaviors suggest a more dramatic effect of weakening adsorption kinetics through k,Da rather than increasing desorptive power via Bi.

3.3. Multi-drop surfactant-laden dispersion

In this brief exploratory section, we consider a short version of the parametric study conducted above for a more

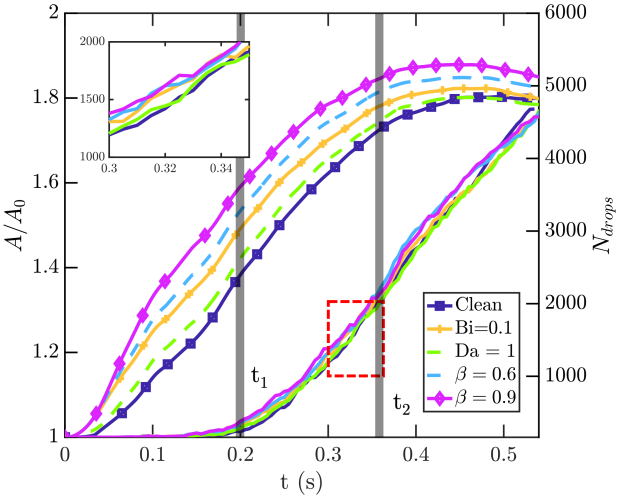

Figure 13: Comparative temporal evolution of the normalized interfacial area A/A_0 (left axis) and number of detached structures N_{drops} (right axis) for different surfactant physicochemical profiles considering a multi-drop set-up specified in §2.1. Highlighted times t_1, t_2 refer to instances shown in Fig. 14.

industrially-relevant multi-drop inlet, as described in Valdes et al. [1] (coarse per-mix setup). To avoid redundancy, the main trends behind dispersion performance will be highlighted, while diving into physical mechanisms sparingly, as they can be directly extrapolated from the aforementioned dynamics.

Fig. 13 illustrates a clear distinction between the interfacial growth attained with different surfactant physicochemical profiles. Following the discussion given in §3.2, the insoluble cases exhibit the highest A/A_0, which ultimately ascends at higher β, considering the intricacies behind competing processes stemming from $\uparrow \frac{\partial \tilde{\sigma}}{\partial \tilde{\Gamma}}$ (greater shear-driven deformation due to $\downarrow \tilde{\sigma}$ vs. augmented interfacial retraction from $\uparrow \tau_M$) [18, 19, 28]. The soluble scenarios lie between the insoluble and clean deformation profiles [30, 31], with the weakest adsorption kinetics aligning closer to the clean curve. The transition between stages (i.e., inflection point) and other distinctive features associated with specific deformational dynamics (i.e., undulations related to forking and wrapping) are smoothed out from the A/A_0 curves due to the layered configuration of incoming droplets, which causes several mechanisms to progress simultaneously (i.e., drops from different layers breaking, wrapping and elongating) [1].

By isolating sections where A/A_0 behaves quasi-linearly, the timeframe between t(s) $\in [0, 0.1]$ depicts quite rich variations between different systems. $\frac{\Delta A/A_0}{\Delta t}$ rises by $\Delta \approx 1.08\text{s}^{-1}$ from the clean to the Bi=0.1 case, namely from $G_{clean} \approx 1.42\text{s}^{-1}$ to $G_{Bi} \approx 2.50\text{s}^{-1}$, with Da=1 roughly in the middle at $G_{Da} \approx 1.83\text{s}^{-1}$. On the other hand, a higher increment of $\Delta \approx 1.37\text{s}^{-1}$ takes place between the clean and insoluble, with an even larger gap existing to the highest elasticity, spiking from $G_{\beta=0.6} \approx 2.79\text{s}^{-1}$ to $G_{\beta=0.9} \approx 3.34\text{s}^{-1}$. All cases seem to stabilize between t(s) $\in [0.1, 0.3]$ at an average rate of $\approx 2.32\text{s}^{-1}$, implying a saturation of the system

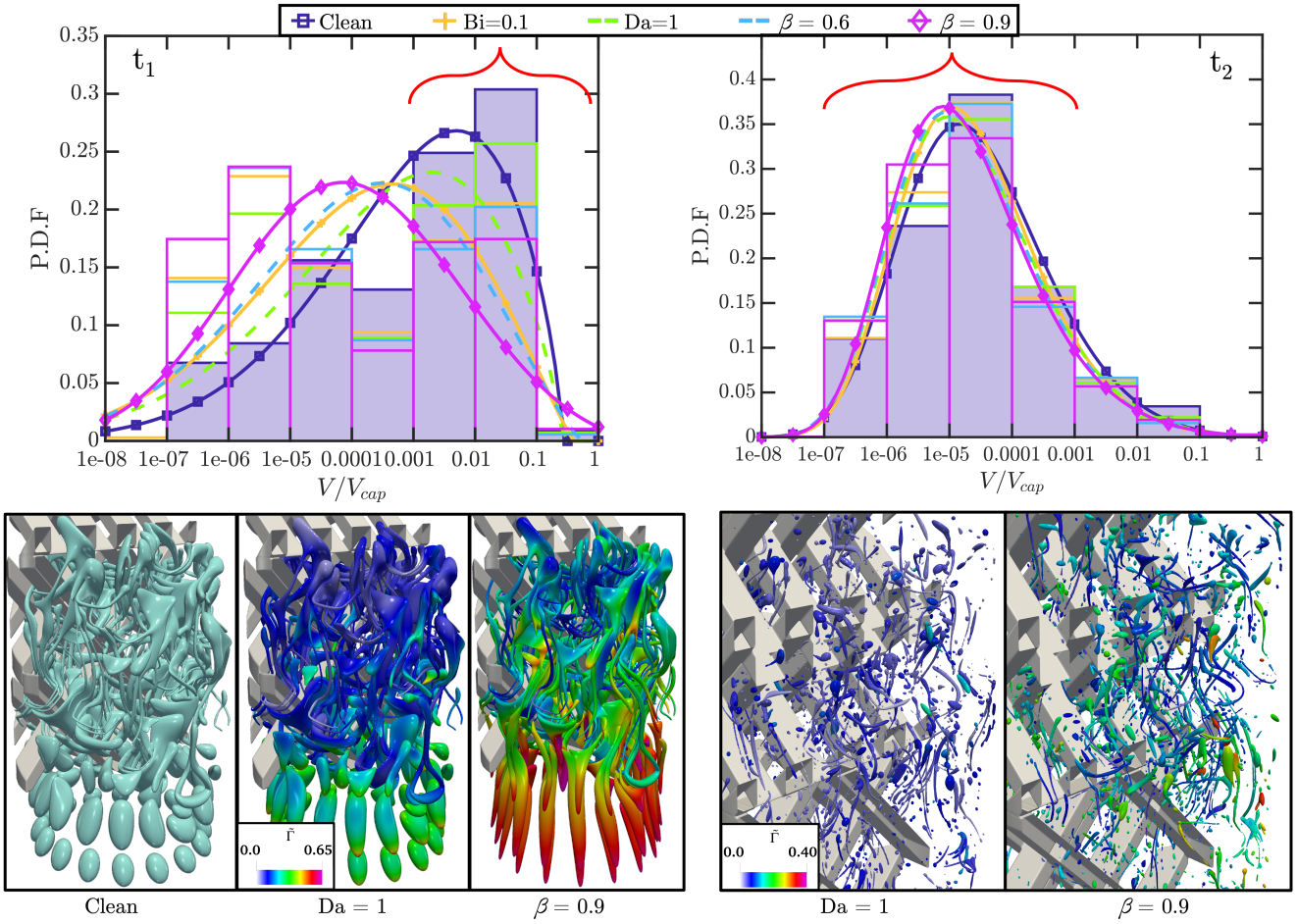

Figure 14: Comparative dimensionless DSDs in the top row for times t_1 (left) and t_2 (right) identified in Fig. 13. The DSDs are represented through a normalized probability histogram with a superimposed PDF curve. All multi-drop cases, at both t_1, t_2, are fitted to a generalized extreme value distribution to better capture the sparsity of the data in the different size groups. Bottom row emphasizes on the dispersed phase's morphology of selected cases (clean, weakly adsorptive and insoluble) at each temporal instance. Drops shown correspond to a subset of the drop population marked with red brackets on the histogram plot.

where modifying surfactant properties will no longer have a substantial effect on interfacial deformation.

Fig. 13 also displays the evolution of the droplet count, which for all scenarios, including the clean, collapses to a dimensionless generalized logistic function, obeying the expression $\tilde{N}_d = \frac{1.089}{1+e^{-7.231(\tilde{t}-0.6927)}}$ with an $R^2 = 0.9920$. Moreover, fitting each case separately leads to a similar result, where the M and k_g parameters present minimal relative variation, ranging between $5153 < M < 5484$ and $12.33 < k_g < 13.27$. These outcomes reinforce the observation raised above on the saturated state of the dispersion after $t > 0.1$s, since droplet births will not depend predominantly on the nature of the surfactant, but rather on the average energy imparted by the mixer [1]. This phenomenon is an inherent consequence of the high oil phase volume fraction travelling through an insufficiently long mixer. As depicted in the 3D views in Fig. 14 @t_1, large drops promptly fill the SMX element as they elongate and wrap around crossbars, severely disrupting the internal hydrodynamics. This potentially intensifies the shear experienced by the drops, analogous to modifying the continuous phase's effective viscosity [2, 47], thus obscuring variations in the drop production stemming from the surfactant's properties. Nevertheless, the A/A_0 at the exit region ($t > 0.4$s) plateaus at markedly different values for each case, adhering to the trends established in §3.2. This indicates distinct degrees of interfacial distortion, dependent on the surfactant's nature, which could favour particular breakup modes if the dispersion was to continue.

Notwithstanding, heterogeneity in breakup events at different physicochemical profiles can be identified throughout the dispersion, despite being concealed by the deceptively large drop count scale. The top-left close-up in Fig. 13 at t(s) $\in [0.3, 0.35]$ reveals a gap of $\sim$ 100+ drops between the clean and Bi=0.1 system, which is doubled when compared against the $\beta = 0.9$ case, being consistent with the drop count deviations estimated in §3.2. In addition, substantial impact on the DSDs is captured in Fig. 14 at t_1, in agreement with the A/A_0 disparities at $t < 0.1$s. Considering the sparsity of the data across different size groups at this early stage, DSDs were fitted to a generalized extreme value (GEV) dis-

tribution via Q-Q plot analysis, seeking to best represent the inhomogeneities in the distributions. Stronger and/or less soluble surfactants enhance the production of small-sized drops and prompt higher variability, thereby generating wider and left-shifted distribution bells with a faint yet positive skewness ($0.075 < s < 0.195$). On the contrary, the clean and highly soluble Da=1 case show an emphatic right-shift with a thin yet long left tail ($s_{clean} < s_{\mathrm{Da}} = -0.18$), implying a greater population of unbroken large structures.

Due to the sparsity of the data, all distributions exhibit a platykurtic modality ($k_{ex} < 0$), indicating lighter, less populated tails. Therefore, the skewness features discussed in §3.2 are not directly comparable, given the dissimilar nature of the DSDs therein. Distributions at t_2 illustrate gentler contrasts, while still preserving the same trends. Systems with stronger surfactant activity induce heavier left-tails and wider distribution spans. The 3D bottom views @t_2 show comparable drop populations with markedly different $\tilde{\Gamma}$, exemplifying the saturation effect but showcasing the underlying contrasts in surfactant content. These complex scenarios successfully extrapolate the main results gathered throughout this paper, clearly identifying the impact in performance of varying surfactant properties, even at highly saturated, hydrodynamically disrupted systems.

4. Conclusions

A numerical investigation of the fundamental physical mechanisms governing surfactant-laden L-L dispersions in a SMX mixer has been conducted using high fidelity, 3D direct numerical simulations coupled with an interface tracking algorithm. Furthermore, a parametric study was carried out to elucidate the effect of different surfactant physicochemical profiles in the dispersion performance, aiming to extrapolate the main trends to more realistic case studies.

Deformational mechanisms are dictated by two competing effects: 1) inhomogeneity in capillary forces induced by local $\tilde{\sigma}$ fluctuations, and 2) Marangoni stresses arising from surface concentration gradients ($\nabla_s\tilde{\Gamma}$), modulated by the sensitivity between $\tilde{\sigma} - \tilde{\Gamma}$ ($\frac{\partial\tilde{\sigma}}{\partial\tilde{\Gamma}}$). The importance of these effects greatly depends on the local hydrodynamics. Shearing type flows ($Q = 0$) developing at high strain regions near the crossbars/cross-points, and strong inertial flows mostly emerging at the center of corridors, nullify τ_M action since they grant sufficiently high interfacial velocities to allow for surface flux, even at high $\tilde{\Gamma} >> 0.5$, thus enabling mechanisms contingent on surfactant accumulation to unfold (i.e., tip-stretching). Contrarily, Marangoni plays an influential role in prevailing extensional ($Q = 1$) and weakly inertial flows (e.g., recirculation regions).

Surfactant-induced effects reveal a dual nature:

- Prompting a more unstable interface susceptible to larger distortions. This effect is associated with weaker restoring interfacial forces ($\downarrow \tilde{\sigma}$), which enhance shear-driven splitting events spawning new necks, and accelerate elongation via tip-stretching due to surfactant accumulating at the forming lobes.
- Stabilizing deformational dynamics by limiting interfacial spread, and preventing early breakups. This effect comes two-fold, firstly from surfactant dilution during wrapping, being swept towards the nascent poles, thus triggering a rise in $\tilde{\sigma}$ at the point of contact; and secondly, Marangoni stresses retracting and rigidifying interfacial regions primarily subjected to extensional deformation, thereby restricting interfacial spread and generating thinner and longer ligaments.

These observations can translate to the breakage mechanisms, which, in conjunction with the local characteristics of the interfacial entity (i.e., $\tilde{L}_0$, Oh, fluid-solid interaction), ultimately dictate the breakup mode occurring. Marangoni flows exhibit a two-pronged effect in relation to breakup events, conditional to their relative strength/activity against disruptive external stresses. They can act beneficially and augment small drop formation (i.e., stabilizing ligament lengthening, hence favouring high output breakup modes), or detrimentally and restrict droplet birth altogether (i.e., delaying or precluding pinch-off and accelerating ligament retraction).

The parametric study reflected a consistent trend throughout: stronger surfactant activity, determined by either elevated elasticities (β) or weaker bulk solubility (highly adsorptive/weakly desorptive), yields a larger interfacial area growth and higher droplet count with a left-biased DSD, leaning towards small-sized droplets with a wider degree of variability. As dissected from the underlying physics, adding surfactant tends to promote sizeable populations of large $\tilde{L}_0$ ligaments, thus favouring high output breakup modes rendering more, smaller droplets. Variability is introduced via augmenting τ_M effects, which alters breakup mechanisms as mentioned prior. Solubility effects trigger a shift in the predominant breakup modes, which is detected by a deviation from the logistic evolution of the droplet count and a departure from a Gaussian distribution of the DSD. Weakening the adsorptive profile suggested a more dramatic effect compared to rising desorption relevance vs. surface convection.

The perspectives presented herein, to our knowledge, deliver a valuable first account of the complex governing interfacial dynamics behind an industrially-relevant surfactant-laden system by offering an unprecedented level of detail, currently inaccessible via numerical volume-averaged or experimental methods. These results can substantially benefit decision-making pipelines in operation and equipment design by providing a comprehensive physical understanding of the implications behind surfactant physicochemical properties, visualized from relevant dispersion performance metrics. Furthermore, the physical insights showcased can serve as building blocks for the development of more robust predictive models and correlations that can offer wider applicability and improved accuracy.

Acknowledgements

This work is supported by the Engineering and Physical Sciences Research Council, United Kingdom, through the EPSRC Programme Grants, MEMPHIS (EP/K003976/1) and

PREMIERE (EP/T000414/1). This work is also supported by the Colombian Minisitry of Science, Technology and Innovation, *MINCIENCIAS*, through a doctoral studentship for JV. O.K.M. acknowledges the Royal Academy of Engineering for a Research Chair in Multiphase Fluid Dynamics. We also acknowledge the HPC facilities provided by the Research Computing Service (RCS) of Imperial College London. D.J. and J.C. acknowledge support through computing time at the Institut du Developpement et des Ressources en Informatique Scientifique (IDRIS) of the Centre National de la Recherche Scientifique (CNRS), coordinated by Grand Equipement National de Calcul Intensif (GENCI) Grant 2023 A0142B06721. Simulations have been performed using code BLUE [41].

References

[1] J. P. Valdes, L. Kahouadji, F. Liang, S. Shin, J. Chergui, D. Juric, and O. K. Matar, "Direct numerical simulations of liquid–liquid dispersions in a SMX mixer under different inlet conditions," Chemical Engineering Journal, vol. 462, p. 142248, 4 2023.

[2] J. P. Valdés, L. Kahouadji, and O. K. Matar, "Current advances in liquid–liquid mixing in static mixers: A review," Chemical Engineering Research and Design, vol. 177, 1 2022.

[3] F. Leal-Calderon, J. Bibette, and V. Schmitt, Emulsion science: Basic principles, 2nd ed. Springer, 2007.

[4] L. Fradette, B. Brocart, and P. A. Tanguy, "Comparison of mixing technologies for the production of concentrated emulsions," Chemical Engineering Research and Design, 2007.

[5] A. Håkansson, "Emulsion Formation by Homogenization: Current Understanding and Future Perspectives," Annual Review of Food Science and Technology, vol. 10, pp. 239–258, 2019.

[6] E. Lobry, F. Theron, C. Gourdon, N. Le Sauze, C. Xuereb, and T. Lasuye, "Turbulent liquid-liquid dispersion in SMV static mixer at high dispersed phase concentration," Chemical Engineering Science, 2011.

[7] R. K. Thakur, C. Vial, K. D. Nigam, E. B. Nauman, and G. Djelveh, "Static mixers in the process industries - a review," Chemical Engineering Research and Design, vol. 81, no. 7, pp. 787–826, 2003.

[8] M. D. Das, A. N. Hrymak, and M. H. Baird, "Laminar liquid-liquid dispersion in the SMX static mixer," Chemical Engineering Science, 2013.

[9] F. Theron, N. Le Sauze, and A. Ricard, "Turbulent liquid-liquid dispersion in sulzer SMX mixer," Industrial and Engineering Chemistry Research, 2010.

[10] S. Middleman, "Drop Size Distributions Produced by Turbulent Pipe Flow of Immiscible Fluids through a Static Mixer," Industrial and Engineering Chemistry Process Design and Development, 1974.

[11] F. Streiff, "In-line dispersion and mass transfer using static mixing equipment," 1977.

[12] H. P. Grace, "Dispersion phenomena in high viscosity immiscible fluid systems and application of static mixers as dispersion devices in such systems," Chemical Engineering Communications, 1982.

[13] P. D. Berkman and R. V. Calabrese, "Dispersion of viscous liquids by turbulent flow in a static mixer," AIChE Journal, 1988.

[14] P. A. Haas, "Turbulent dispersion of aqueous drops in organic liquids," AIChE Journal, 1987.

[15] Y. F. Maa and C. Hsu, "Liquid-liquid emulsification by static mixers for use in microencapsulation," Journal of Microencapsulation, 1996.

[16] J. Legrand, P. Morançais, and G. Carnelle, "Liquid-liquid dispersion in an SMX-Sulzer static mixer," Chemical Engineering Research and Design, 2001.

[17] J. P. Gingras, L. Fradette, P. Tanguy, and J. Bousquet, "Inline bitumen emulsification using static mixers," in Industrial and Engineering Chemistry Research, 2007.

[18] Y. Pawar and K. J. Stebe, "Marangoni effects on drop deformation in an extensional flow: The role of surfactant physical chemistry. I. Insoluble surfactants," Physics of Fluids, vol. 8, no. 7, pp. 1738–1751, 7 1996.

[19] X. Li and C. Pozrikidis, "The effect of surfactants on drop deformation and on the rheology of dilute emulsions in Stokes flow," Journal of Fluid Mechanics, vol. 341, pp. 165–194, 6 1997.

[20] C. D. Eggleton, Y. P. Pawar, and K. J. Stebe, "Insoluble surfactants on a drop in an extensional flow: a generalization of the stagnated surface limit to deforming interfaces," Journal of Fluid Mechanics, vol. 385, pp. 79–99, 4 1999.

[21] K. Feigl, D. Megias-Alguacil, P. Fischer, and E. J. Windhab, "Simulation and experiments of droplet deformation and orientation in simple shear flow with surfactants," Chemical Engineering Science, vol. 62, no. 12, pp. 3242–3258, 6 2007.

[22] G. Soligo, A. Roccon, and A. Soldati, "Deformation of clean and surfactant-laden droplets in shear flow," Meccanica, vol. 55, no. 2, pp. 371–386, 2 2020.

[23] H. A. Stone and L. G. Leal, "The effects of surfactants on drop deformation and breakup," Journal of Fluid Mechanics, vol. 220, pp. 161–186, 11 1990.

[24] W. J. Milliken, H. A. Stone, and L. G. Leal, "The effect of surfactant on the transient motion of Newtonian drops," Physics of Fluids A: Fluid Dynamics, vol. 5, no. 1, pp. 69–79, 1 1993.

[25] C. D. Eggleton, T.-M. Tsai, and K. J. Stebe, "Tip Streaming from a Drop in the Presence of Surfactants," Physical Review Letters, vol. 87, no. 4, p. 048302, 7 2001.

[26] Y. W. Kruijt-Stegeman, F. N. van de Vosse, and H. E. H. Meijer, "Droplet behavior in the presence of insoluble surfactants," Physics of Fluids, vol. 16, no. 8, pp. 2785–2796, 8 2004.

[27] J. J. M. Janssen, A. Boon, and W. G. M. Agterof, "Influence of dynamic interfacial properties on droplet breakup in plane hyperbolic flow," AIChE Journal, vol. 43, no. 6, pp. 1436–1447, 6 1997.

[28] I. B. Bazhlekov, P. D. Anderson, and H. E. Meijer, "Numerical investigation of the effect of insoluble surfactants on drop deformation and breakup in simple shear flow," Journal of Colloid and Interface Science, vol. 298, no. 1, pp. 369–394, 6 2006.

[29] J. Janssen, A. Boon, and W. Agterof, "Droplet break-up in simple shear flow in the presence of emulsifiers," Colloids and Surfaces A: Physicochemical and Engineering Aspects, vol. 91, pp. 141–148, 11 1994.

[30] W. J. Milliken and L. Leal, "The Influence of Surfactant on the Deformation and Breakup of a Viscous Drop: The Effect of Surfactant Solubility," Journal of Colloid and Interface Science, vol. 166, no. 2, pp. 275–285, 9 1994.

[31] C. D. Eggleton and K. J. Stebe, "An Adsorption–Desorption-Controlled Surfactant on a Deforming Droplet," Journal of Colloid and Interface Science, vol. 208, no. 1, pp. 68–80, 12 1998.

[32] F. Jin, N. R. Gupta, and K. J. Stebe, "The detachment of a viscous drop in a viscous solution in the presence of a soluble surfactant," Physics of Fluids, vol. 18, no. 2, p. 022103, 2 2006.

[33] F. Jin and K. J. Stebe, "The effects of a diffusion controlled surfactant on a viscous drop injected into a viscous medium," Physics of Fluids, vol. 19, no. 11, p. 112103, 11 2007.

[34] M. Rubio and J. Montanero, "Influence of a soluble surfactant on the transition to tip streaming," Experimental Thermal and Fluid Science, vol. 141, p. 110776, 2 2023.

[35] Y.-C. Liao, E. I. Franses, and O. A. Basaran, "Deformation and breakup of a stretching liquid bridge covered with an insoluble surfactant monolayer," Physics of Fluids, vol. 18, no. 2, p. 022101, 2 2006.

[36] P. M. Kamat, B. W. Wagoner, S. S. Thete, and O. A. Basaran, "Role of Marangoni stress during breakup of surfactant-covered liquid threads: Reduced rates of thinning and microthread cascades," Physical Review Fluids, vol. 3, no. 4, p. 043602, 4 2018.

[37] P. M. Kamat, B. W. Wagoner, A. A. Castrejón-Pita, J. R. Castrejón-Pita, C. R. Anthony, and O. A. Basaran, "Surfactant-driven escape from endpinching during contraction of nearly inviscid filaments," Journal of Fluid Mechanics, vol. 899, p. A28, 9 2020.

[38] A. Martínez-Calvo, J. Rivero-Rodríguez, B. Scheid, and A. Sevilla,

"Natural break-up and satellite formation regimes of surfactant-laden liquid threads," Journal of Fluid Mechanics, vol. 883, p. A35, 1 2020.
[39] C. R. Constante-Amores, L. Kahouadji, A. Batchvarov, S. Shin, J. Chergui, D. Juric, and O. K. Matar, "Dynamics of retracting surfactant-laden ligaments at intermediate Ohnesorge number," Physical Review Fluids, vol. 5, no. 8, p. 084007, 8 2020.
[40] S. Shin and D. Juric, "A hybrid interface method for three-dimensional multiphase flows based on front tracking and level set techniques," International Journal for Numerical Methods in Fluids, vol. 60, no. 7, 7 2009.
[41] S. Shin, J. Chergui, and D. Juric, "A solver for massively parallel direct numerical simulation of three-dimensional multiphase flows," Journal of Mechanical Science and Technology, vol. 31, no. 4, 4 2017.
[42] S. Shin, J. Chergui, D. Juric, L. Kahouadji, O. K. Matar, and R. V. Craster, "A hybrid interface tracking – level set technique for multiphase flow with soluble surfactant," Journal of Computational Physics, vol. 359, pp. 409–435, 4 2018.
[43] S. Liu, A. N. Hrymak, and P. E. Wood, "Drop breakup in an SMX static mixer in laminar flow," Canadian Journal of Chemical Engineering, 2005.
[44] B. Andersson, R. Andersson, L. Håkansson, M. Mortensen, R. Sudiyo, and B. Van Wachem, Computational fluid dynamics for engineers, 2011, vol. 9781107018.
[45] A. Batchvarov, L. Kahouadji, M. Magnini, C. R. Constante-Amores, S. Shin, J. Chergui, D. Juric, R. V. Craster, and O. K. Matar, "Effect of surfactant on elongated bubbles in capillary tubes at high Reynolds number," Physical Review Fluids, vol. 5, no. 9, 9 2020.
[46] M. Muradoglu and G. Tryggvason, "Simulations of soluble surfactants in 3D multiphase flow," Journal of Computational Physics, vol. 274, pp. 737–757, 10 2014.
[47] E. W. Barega, E. Zondervan, and A. B. De Haan, "Influence of physical properties and process conditions on entrainment behavior in a static-mixer settler setup," Industrial and Engineering Chemistry Research, 2013.
[48] G. A. Farzi, N. Rezazadeh, and A. P. Nejad, "Droplet Formation Study in Emulsification Process by KSM using a Novel In Situ Visualization System," Journal of Dispersion Science and Technology, vol. 37, pp. 575–581, 2016.
[49] S. I. Karakashev and A. V. Nguyen, "Effect of sodium dodecyl sulphate and dodecanol mixtures on foam film drainage: Examining influence of surface rheology and intermolecular forces," Colloids and Surfaces A: Physicochemical and Engineering Aspects, vol. 293, no. 1-3, pp. 229–240, 2 2007.
[50] A. Siderius, S. K. Kehl, and D. G. Leaist, "Surfactant diffusion near critical micelle concentrations," Journal of Solution Chemistry, vol. 31, no. 8, pp. 607–625, 2002.
[51] C. Constante-Amores, A. Batchvarov, L. Kahouadji, S. Shin, J. Chergui, D. Juric, and O. Matar, "Role of surfactant-induced Marangoni stresses in drop-interface coalescence," Journal of Fluid Mechanics, vol. 925, p. A15, 10 2021.
[52] H. Manikantan and T. M. Squires, "Surfactant dynamics: hidden variables controlling fluid flows," Journal of Fluid Mechanics, vol. 892, p. P1, 6 2020.
[53] C.-H. Chang and E. I. Franses, "Adsorption dynamics of surfactants at the air/water interface: a critical review of mathematical models, data, and mechanisms," Colloids and Surfaces A: Physicochemical and Engineering Aspects, vol. 100, pp. 1–45, 7 1995.
[54] A. A. Levchenko, B. P. Argo, R. Vidu, R. V. Talroze, and P. Stroeve, "Kinetics of Sodium Dodecyl Sulfate Adsorption on and Desorption from Self-Assembled Monolayers Measured by Surface Plasmon Resonance," Langmuir, vol. 18, no. 22, pp. 8464–8471, 10 2002.
[55] B. Li, G. Geeraerts, and P. Joos, "Kinetic equations for transfer-controlled adsorption kinetics," Colloids and Surfaces A: Physicochemical and Engineering Aspects, vol. 88, no. 2-3, pp. 251–266, 9 1994.
[56] Y. He, P. Yazhgur, A. Salonen, and D. Langevin, "Adsorption–desorption kinetics of surfactants at liquid surfaces," Advances in Colloid and Interface Science, vol. 222, pp. 377–384, 8 2015.
[57] P. Joos and G. Serrien, "Adsorption kinetics of lower alkanols at the air/water interface: Effect of structure makers and structure breakers," Journal of Colloid and Interface Science, vol. 127, no. 1, pp. 97–103, 1 1989.
[58] B. J. Bentley and L. G. Leal, "An experimental investigation of drop deformation and breakup in steady, two-dimensional linear flows," Journal of Fluid Mechanics, vol. 167, no. -1, 6 1986.
[59] L. Kahouadji, F. Liang, J. P. Valdes, S. Shin, J. Chergui, D. Juric, R. V. Craster, and O. K. Matar, "The transition to aeration in turbulent two-phase mixing in stirred vessels," Flow, vol. 2, p. E30, 10 2022.
[60] F. Liang, L. Kahouadji, J. P. Valdes, S. Shin, J. Chergui, D. Juric, and O. K. Matar, "Numerical study of oil–water emulsion formation in stirred vessels: effect of impeller speed," Flow, vol. 2, p. E34, 11 2022.
[61] C. Constante-Amores, L. Kahouadji, A. Batchvarov, S. Shin, J. Chergui, D. Juric, and O. Matar, "Direct numerical simulations of transient turbulent jets: vortex-interface interactions," Journal of Fluid Mechanics, vol. 922, p. A6, 9 2021.
[62] H. Zhao, W.-B. Zhang, J.-L. Xu, W.-F. Li, and H.-F. Liu, "Surfactant-laden drop jellyfish-breakup mode induced by the Marangoni effect," Experiments in Fluids, vol. 58, no. 3, p. 13, 3 2017.
[63] F. Wang, F. P. Contò, N. Naz, J. R. Castrejón-Pita, A. A. Castrejón-Pita, C. G. Bailey, W. Wang, J. J. Feng, and Y. Sui, "A fate-alternating transitional regime in contracting liquid filaments," Journal of Fluid Mechanics, vol. 860, pp. 640–653, 2 2019.
[64] T. Driessen, R. Jeurissen, H. Wijshoff, F. Toschi, and D. Lohse, "Stability of viscous long liquid filaments," Physics of Fluids, vol. 25, no. 6, p. 062109, 6 2013.
[65] P. K. Notz and O. A. Basaran, "Dynamics and breakup of a contracting liquid filament," Journal of Fluid Mechanics, vol. 512, 8 2004.
[66] B. Silverman, Density Estimation for Statistics and Data Analysis, 1st ed. London: Chapman & Hall, 1986.